ACS APPLIED ENERGY MATERIALS

www.acsaem.org

Article

Insights into the Mechanism-Dependent Efficiency of the Electrocatalytic Oxygen Evolution Reaction on Octacarboxyphthalocyanine-Based Coordination Polymers

Ítalo R. Machado, Raphael P. Bacil,* Victor Vendruscolo, Rafael M. Buoro, Helton P. Nogueira, Robson R. Guimarães, Sergio H. Toma, Márcia C. A. Fantini, Josué M. Gonçalves, and Koiti Araki*

Cite This: https://doi.org/10.1021/acsaem.4c02297

Read Online

ACCESS | Metrics & More | Article Recommendations | Supporting Information

ABSTRACT: Cobalt and iron octacarboxyphthalocyanines based $M_aOcPc\text{-}M_b$-type coordination polymers (where M_a = Fe^{2+} or Co^{2+}, and M_b = Fe^{2+}, Co^{2+}, or Ni^{2+}) were prepared and characterized and their oxygen evolution reaction electrocatalytic properties carefully evaluated using an experimental/theoretical approach. FeOcPc-Ni stands out among them as the electrocatalyst with the best performance, as confirmed by the low overpotential (η_{10} = 299 mV at ν = 0.020 V s^{-1}) and Tafel slope (46.4 mV dec^{-1}), results that were reinforced by additional parameters from Tafel, foot of the wave, turnover frequency, and electrochemical impedance spectroscopy analyses. The reaction mechanism was found to involve the formation of a peroxide intermediate where the rate-determining step can be either (a) the adsorption of the substrate (hydroxide ion or water) or (b) the regeneration of the catalyst at the end of the OER process in a competitive fashion. Turnover frequency analysis combined with foot of the wave analysis was shown to be a powerful tool, especially when associated with the analyses of the voltammetric and electrochemical impedance spectroscopy profiles, to evaluate the performance and mechanism of electrocatalytic materials. Both the bridging ligand and the macrocyclic ring-coordinated transition metal were shown to contribute synergic effects, boosting the electrocatalytic properties of the FeOcPc-Ni coordination polymer and increasing its potential as an oxidation electrocatalyst to close the circuit in reduction processes in aqueous media, such as hydrogen gas production by water splitting, nitrogen and CO_2 reduction to ammonia, and processes involving low-molecular-weight hydrocarbons.

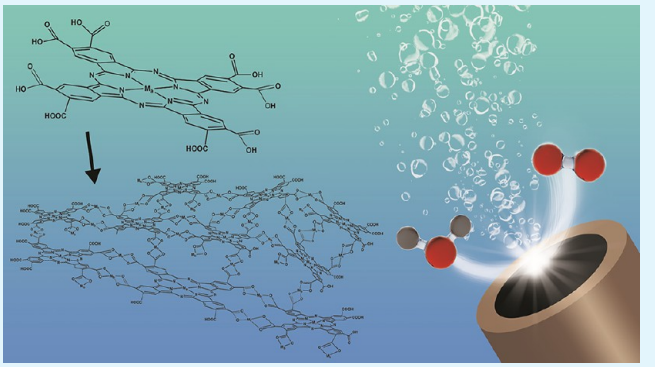

KEYWORDS: *Oxygen Evolution Reaction, Phthalocyanines, Coordination Polymers, Electrocatalysis, Reaction Mechanism, Proton-Coupled Electron Transfer*

INTRODUCTION

Our planet faces urgent environmental challenges such as acid rain, ozone layer depletion, and the escalating greenhouse effect. These issues stem from our heavy reliance on fossil fuels, which drives up global temperatures and triggers extreme climate events. To avert catastrophe, we must prioritize environmentally friendly energy conversion and storage technologies.[1−3]

In this context, hydrogen fuel cells are promising energy alternatives since they allow converting the energy stored as hydrogen or ammonia gas, using solar, wind, and hydroelectric alternative sources, back to electricity,[4] producing harmless water molecules that could be used as a hydric source in arid regions.[5] Despite the rise of this promising solution, it is expected that only about 10% of the needed global energy would be provided by hydrogen sources, with less than 5% coming from renewable sources,[6,7] since efficient hydrogen generation remains a challenge.

Among renewable options, electrochemical water-splitting stands out, as this technology relies on water electrolysis to generate H_2,[8] but a bottleneck lies in the simultaneous O_2 evolution process at the counter electrode. In essence, water-splitting depends on two complementary semi-reactions: the oxygen evolution reaction (OER) and the hydrogen evolution reaction (HER).[9] Given the involvement of innocuous small molecules such as H_2O and O_2, the OER apparently seems to be a simple reaction but in fact it poses a formidable obstacle for commercial viability.[10] Its slow kinetics and high overpotentials come from the complex reaction mechanism,

Received: September 7, 2024
Revised: September 24, 2024
Accepted: September 27, 2024

depending on the transfer of four electrons coupled to four protons and formation of a O═O bond, taking place in several steps (Scheme 1). In this type of mechanism, the activation

Scheme 1. Possible Mechanisms of Catalyzed Oxygen Evolution Reactions in Acidic (Purple) and Alkaline (Orange) Media, Showing the Formation of Molecular Oxygen Directly from the Reaction of Two Oxo Intermediates (M−O) (Green) and the Peroxide Pathway (M−OOH) (Black)

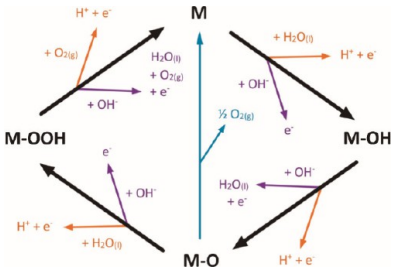

energy for the reaction tends to sum-up at each step until reaching the rate-determining step (RDS). The several steps and high activation energy explain its sluggishness, making it an interesting challenge and providing an opportunity to find new electrocatalysts to speed up that semi-reaction. Thus, the efficiency of the OER, whose mechanisms in acidic and alkaline media are depicted in Table 1 and Scheme 1, must be significantly improved to make the water-splitting reaction economically affordable as a fuel source.[11]

Noble-metal-based compounds were the first commercially available OER catalysts, and since then RuO_2- and IrO_2-based materials have become the reaction benchmarks,[13−15] despite their low abundance and high costs, which inhibit large-scale production and broad accessibility to the technology. Under elevated anodic potentials, however, both RuO_2 and IrO_2 form high-valence oxides such as RuO_4 and IrO_6, responsible for the lixiviation of those materials from the electrode surface into the electrolyte solution, continuously slowing down the catalyzed reaction.[16−18]

In the quest for low-cost and high-performance catalysts, materials based on first transition series metal oxides and hydroxides have emerged as promising OER catalysts, thanks to the possibility of accessing multiple oxidation states, as well as their abundance and lower cost along with corrosion resistance and good performance. Recently, $M^{2+/3+/4+}$ ions have been found to be the active sites of monometallic materials incorporating Ni, Co, and Fe.[16,19−21] Nevertheless, a wide range of bimetallic, trimetallic, and even polymetallic materials have been prepared in exploring the several cooperative interactions and synergic effects involving different metal species,[12,22] especially iron sites.[23−25] In addition, many efforts have been dedicated to improving the electrocatalytic materials' properties, such as durability and kinetic parameters, exploring not only metal oxides/hydroxides-based materials but also transition metal sulfides, phosphides, nitrides, and organometallic compounds.[26−28]

In this context, the state-of-the-art class of materials known as metallo-organic coordination polymers (CPs) have attracted interest due to their easily tunable properties, high availability of active sites, and enhanced catalytic areas.[29] Such properties result from their structures, in which several metal ions are interconnected by organic bridging ligands, thus extending the structure in one, two, or three dimensions (2D and 3D structures denominate metal−organic frameworks, MOFs).[30,31] Although most of the work in the past decades has focused on crystalline materials, amorphous CPs are showing promising results in distinct fields, including water-splitting and, more specifically, OER catalysis.[32,33]

The properties of CPs are strongly dependent on the metal ions and the ligands, making the choice of a suitable bridging ligand fundamental to provide the desired electrocatalytic activity as well as electronic conduction properties. Accordingly, transition metal complexes of aromatic macrocyclic ligands with well-known electrocatalytic properties, such as porphyrins (P's) and phthalocyanines (Pc's), are among the most promising ones. Focusing on Pc's, they constitute a special class of macrocycles with high thermal stability, chemical stability, and photostability, composed of four isoindol units connected by nitrogen atoms into a ring, generating a tetradentate ligand with an 18 π-electron conjugated aromatic system, which is capable of coordinating more than 70 elements, most of them metal ions. Furthermore, many functional groups and substituents can be attached to the resultant metallophthalocyanines (MPc's) to tune their photonic, electronic, and electrocatalytic properties.[34,35] Therefore, MPc derivatives exhibit photochemical, optical, semiconductor, and electrocatalytic properties and have been extensively explored in applications such as photodynamic therapy, nonlinear optics, and energy conversion devices, among others.[34,36,37] Accordingly, the challenge is designing MPc-based materials with suitable structural and electronic properties, in addition to favorable electronic interactions, to explore their synergic properties.

Table 1. Main Anodic Steps of Catalyzed Oxygen Evolution Reactions in Acidic and Alkaline Media

In acidic electrolyte	In alkaline electrolyte
$2H_2O \rightarrow O_2 + 4H^+ + 4e^-$, $E_0 = +1.23$ V[12]	$4OH^- \rightarrow O_2 + 2H_2O + 4e^-$, $E_0 = -0.40$ V[12]
Reaction mechanism:	**Reaction mechanism:**
$M + H_2O \rightarrow M{-}OH + H^+ + e^-$	$M + H_2O \rightarrow M{-}OH + H^+ + e^-$ or
	$M + OH^- \rightarrow M{-}OH + e^-$
$M{-}OH \rightarrow M{=}O + H^+ + e^-$	$M{-}OH + OH^- \rightarrow M{=}O + H_2O + e^-$
followed by either	**followed by either**
$2M{-}O \rightarrow 2M + O_2 + 2e^-$	$2\ M{=}O \rightarrow 2\ M + O_2 + 2e^-$
or	**or**
$M{=}O + H_2O \rightarrow M{-}OOH + H^+ + e^-$	$M{=}O + OH^- \rightarrow M{-}OOH + e^-$
$M{-}OOH \rightarrow O_2 + H^+ + e^-$	$M{-}OOH + OH^- \rightarrow O_2 + H_2O + e^-$

https://doi.org/10.1021/acsaem.4c02297
ACS Appl. Energy Mater. XXXX, XXX, XXX−XXX

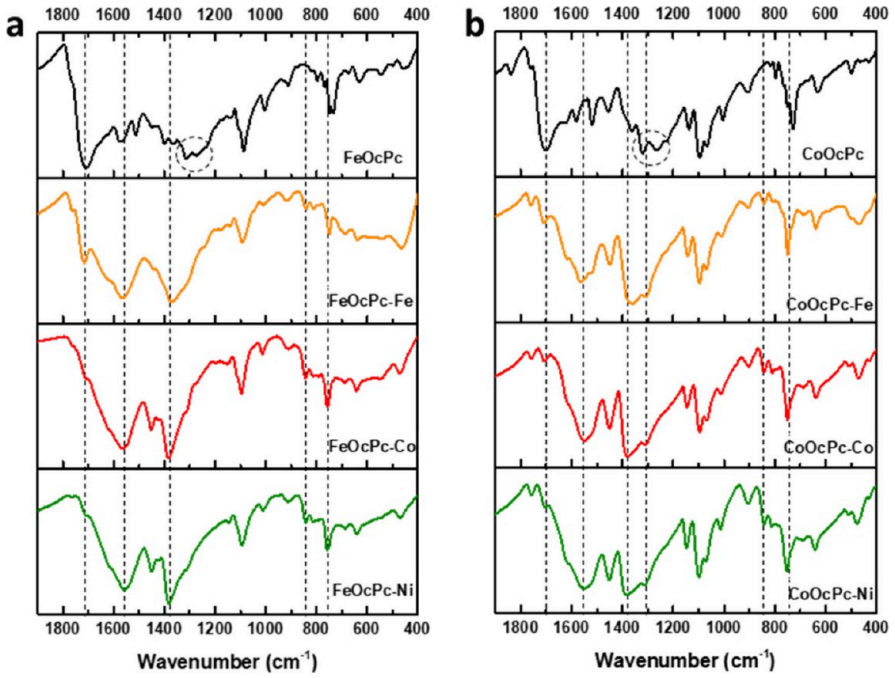

Figure 1. Comparison of the FT-IR spectra of (a) FeOcPc with FeOcPc-Fe, FeOcPc-Co, and FeOcPc-Ni and (b) CoOcPc with CoOcPc-Fe, CoOcPc-Co, and CoOcPc-Ni.

In this context, carboxylate is a well-known coordinating group with good electronic coupling when directly bonded to aromatic molecules forming extended π-systems. In addition, the metal complexes formed as connectors/nodes can be used to tune the CP properties, and vice versa, by coupling a suitable transition metal element and controlling its oxidation state, as well as the coordination sphere around each metal ion.[38−43] However, no CP materials derived from octacarboxyphthalocyanines (MOcPc's) have been reported yet. Hence, this work aims to develop new CP materials from MOcPc's with the highest possible density of transition metal sites to maximize their electrocatalytic performance towards the OER.

MATERIALS AND METHODS

All reagents and solvents were of analytical grade and used as received. Acetone, KOH, HCl, $FeSO_4{\cdot}7H_2O$, and $NiCl_2{\cdot}6H_2O$ were acquired from Synth. $CoCl_2{\cdot}6H_2O$ was obtained from Baker. 1,4-Piperazinediethanesulfonic acid (PIPES buffer) and graphite powder (<150 μm) were purchased from Sigma-Aldrich. Mineral oil was purchased from Tayuyna Lab Ltd. The ring-metalated 2,3,9,10,16,17,23,24-octacarboxyphthalocyanines FeOcPc and CoOcPc (M_aOcPc's where M_a = Fe and Co) were obtained by alkaline hydrolysis of the corresponding iron and cobalt tetraimide phthalocyanines.[44] All aqueous solutions were prepared with ultrapure deionized water from a Millipore Direct-Q 5 UV purification system (DI-water, $\rho \geq 18.2$ MΩ cm).

Preparation of M_aOcPc-M_b Coordination Polymers. A solution of M_aOcPc (M_a = Fe or Co) was prepared by dissolving 200 mg (≈0.216 mmol) of FeOcPc (or CoOcPc) and 242 mg of PIPES buffer (≈0.8 mmol) in 40 mL of a 0.1 mol L^{-1} KOH solution, under vigorous stirring. Then, the pH was adjusted to 7.0 by adding the proper amount of a 0.1 mol L^{-1} of HCl solution. The M_b transition metal ion aqueous solutions were prepared by dissolving 0.545 mmol of $FeSO_4{\cdot}7H_2O$ (150 mg), $CoCl_2{\cdot}6H_2O$ (129.7 mg) and $NiCl_2{\cdot}6H_2O$ (129.5 mg) in 7.5 mL of DI water. In sequence, the M_aOcPc-derived CPs were prepared by dropwise addition of the transition metal ion solution into the buffered M_aOcPc (FeOcPc or CoOcPc) solution under vigorous stirring, resulting in the instantaneous formation of a precipitate. The suspension was then refluxed for 3 h and left to cool down to room temperature. This solution was then centrifuged, and the solid was collected and purified by washing it three times with DI-water and then with acetone. The purified solid was dried overnight at 70 °C, producing six dark granulated M_aOcPc-M_b CP materials, where M_a = Fe or Co, and M_b = Fe^{2+}, Co^{2+} or Ni^{2+}, namely, FeOcPc-Fe, FeOcPc-Co, FeOcPc-Ni, CoOcPc-Fe, CoOcPc-Co, and CoOcPc-Ni.

Characterization of M_aOcPc-M_b Coordination Polymers. All six M_aOcPc-M_b materials were analyzed by FT-IR spectroscopy, and their behaviors were compared with those of FeOcPc and CoOcPc. FT-IR spectra were obtained in a Bruker Alpha spectrophotometer in transmission mode, using samples prepared in KBr pellets (spectroscopic grade, Sigma-Aldrich).

The energy-dispersive X-ray spectroscopy (EDX) analyses were carried out at room temperature in a Shimadzu EDX-720 instrument, equipped with a Rh tube as X-ray source cooled by liquid nitrogen, setting the voltage of the Si(Li) semiconductor detector to 15−50 kV, using powder samples in sample holders with a Mylar film window.

The wide-angle X-ray scattering (WAXS) measurements were performed in Xenocs Xeuss version 1.0 instrument equipped with a copper target GeniX X-ray source (8 keV) and a Dectris Pilatus 100k detector.

Electrochemical Measurements. All electrochemical measurements were performed in an Autolab PGSTAT30 potentiostat/galvanostat using a platinum wire, Ag/AgCl|KCl, 3 mol L^{-1}, and a carbon paste electrode as counter, reference, and working electrodes, respectively. A 0.85 mol L^{-1} KOH solution (experimental pH = 13.9) saturated with N_2 gas was used as the electrolyte.

Carbon Paste Electrode (CPE). The working CPEs were carefully built by mixing 90% graphite powder and 10% mineral oil (m/m) with a pestle in an agate mortar. It is important to notice that the mineral oil is a classic agglutinant to the CPE, which in this case can be used in smaller amounts due to the properties of the CPs that give the electrode the required characteristics to prevent its lixiviation to the solution. This base graphite paste was then loaded with 5 wt% samples based on MPc's and carefully mixed. Altogether, nine electrodes were also prepared: one neat CPE, two loaded respectively with FeOcPc and CoOcPc, and six others with each of the M_aOcPc-M_b CPs. The pastes were placed in the tip of a 2 mm diameter syringe tube, and a brass rod was inserted in the other end, making the

https://doi.org/10.1021/acsaem.4c02297
ACS Appl. Energy Mater. XXXX, XXX, XXX−XXX

electrical contact. Finally, the CPEs were polished by pressing them against a clean flat glass surface until a homogeneous surface was obtained.

The OER activity of each CP material electrode was analyzed by cyclic voltammetry (CV) by sweeping the potential from 0.8 to 2.7 V and back to 0.8 V. Complementarily, a 15 h chronopotentiometry analysis (at 10 mA cm^{-2}) was performed to evaluate the stability of the most active electrode material. Finally, electrochemical impedance spectroscopy (EIS) measurements were carried out to evaluate the behavior of the electrode materials.

The current density (j) was calculated considering the average electrochemical surface area of the neat graphite paste electrode, GphE (0.041 cm^2). All potential data were converted to theoretical reversible hydrogen electrode (RHE) reference considering eq 1, and overpotential (η) values at 10 mA cm^{-2} were determined considering the standard potential of OER as equal to 1.23 V (vs RHE):

$$E_{RHE} = E_{Ag/AgCl} + E^{\circ}_{Ag/AgCl} + 0.059^{\times}pH \quad (1)$$

where E_{RHE} is the potential converted to the RHE reference, $E_{Ag/AgCl}$ is the potential measured experimentally versus Ag/AgCl|KCl 3 M reference electrode, $E^{\circ}_{Ag/AgCl}$ is the standard Ag/AgCl|KCl 3 M potential at 25 °C (0.197 V), and pH is equal to 13.9 in the KOH electrolyte solution.

RESULTS AND DISCUSSION

Characterization of M_aOcPc-M_b CPs. The M_aOcPc macrocyclic complexes are joined together by the formation of bridging carboxylate coordination compounds upon addition of M_b = Fe^{2+}, Co^{2+}, or Ni^{2+}, thus generating the corresponding coordination polymer materials (CPs). Nevertheless, the geometry and the coordination sphere of such bridging Fe^{2+}, Co^{2+}, or Ni^{2+} complexes are not clearly defined, in contrast with the well-defined multibridging CoOcPc and FeOcPc macrocyclic complexes. Accordingly, their structure was characterized by spectroscopic, electrochemical, and thermal analysis techniques, as discussed below.

Fourier Transform Infrared (FT-IR) Spectroscopy. The formation of M_b^{2+}−carboxylate bonds connecting the M_aOcPc molecules in the respective M_aOcPc-M_b CPs should be reflected in their vibrational modes, thus changing the FT-IR spectral profile. Analyzing the FT-IR spectra shown in Figure 1, it is possible to notice that the six M_aOcPc-M_b materials show very similar spectral profiles and changes for the FeOcPc and CoOcPc derivatives within their own groups, as expected for similar interactions with Fe(II), Co(II), and Ni(II) ions, generating the FeOcPc-M_b and CoOcPc-M_b CP-type materials.

As expected, the most affected vibrational modes are the ones related with the carboxylate groups, in which FeOcPc presents a strong C═O stretching band (νC═O) at 1709 cm^{-1} and two similar intensity bands assigned to C−O stretching modes (νC−O) at 1313 and 1273 cm^{-1}, whereas the FeOcPc-M_b derivatives present bands at 1554 ± 13 and 1380 ± 7 cm^{-1}, respectively attributed to the asymmetric and symmetric COO^- stretching modes ($\nu_{as}COO^-$ and $\nu_{sym}COO^-$) (Figure 1a) of metal-ion-coordinated carboxylate groups. Similar behavior was observed for CoOcPc that exhibited a strong νC═O band at 1701 cm^{-1} and two νC−O bands at 1319 and 1263 cm^{-1}, whereas CoOcPc-M_b presented the bands assigned to $\nu_{as}COO^-$ and $\nu_{sym}COO^-$ at 1554 ± 13 cm^{-1} and two at 1375 ± 12 cm^{-1}, with a more well-defined shoulder at 1311 ± 3 cm^{-1}. These results are consistent with our hypothesis of formation of FeOcPc and CoOcPc coordination polymers, as discussed further based on the activation energy of the thermal decarboxylation process. However, it is important to notice that there is a remnant of the carboxylate group νC═O band in all M_aOcPc-M_b materials, especially in FeOcPc-Fe and CoOcPc-Fe, indicating that all carboxylate groups may not be coordinated to the respective transition metal ion, especially when M_b = Fe^{2+}.

These FT-IR profiles associated with the carboxylate group vibrational modes also can provide valuable information about its coordination mode with the metal ion, as reflected by the energy difference of the symmetric and asymmetric stretching modes, $\Delta\nu = \nu_{as}COO^- - \nu_{sim}COO^-$.[48−51] In fact, there are three possibilities (Scheme 2): (i) when $\Delta\nu$ of the complex is larger than $\Delta\nu$ of a free carboxylate group stretching modes ($\Delta\nu_{complex} > \Delta\nu_{free}$), COO^- is coordinated as a monodentate ligand to the metal ion (Scheme 2a); (ii) when $\Delta\nu_{complex} < \Delta\nu_{free}$, COO^- is coordinated to the metal as a bidentate ligand (Scheme 2b); and (iii) when $\Delta\nu_{complex}$ is similar to $\Delta\nu_{free}$, the COO^- group is probably acting as a bridging ligand between two metal ions (Scheme 2c).

Scheme 2. Schematic Representation of the Three Possible Carboxylate Ligand Coordination Modes with a Metal Ion: (a) Monodentate, (b) Bidentate, and (c) Bridging Mode

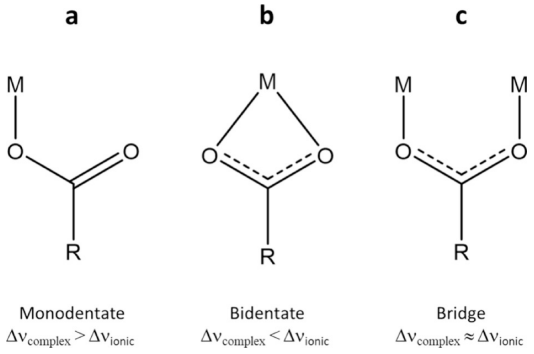

Accordingly, the FT-IR spectra of CoOcPc-M_b are typical of materials with carboxylate groups acting as bidentated ligands (Figure 1), since $\Delta\nu_{free}$ = 210 cm^{-1} (of K_8[CoOcPc]) is larger than the average $\Delta\nu_{complex}$ = 179 cm^{-1}. Therefore, there should be, on average, a M_b metal ion per each vicinal carboxylate group in CoOcPc-M_b, considering that they are shared by two molecules in the solid. Additional relevant information that can be obtained by comparing the FT-IR spectra of similar compounds is about how the aromatic macrocyclic rings may be arranged in the solid. A more ordered and crystalline structure can lead to H-type aromatic ring interactions and the appearance of out-of-plane bending modes in the spectral pattern. For example, FeOcPc and CoOcPc should have less constrained movement than the respective M_aOcPc-M_b CP materials, where the molecules are connected to each other through the four corners, and should form a more organized structure, thus showing two close vibrational bands at 740 cm^{-1}.[52] In contrast, the M_aOcPc-M_b CP materials present one band at 754 ± 6 cm^{-1} and another at 842 ± 1 cm^{-1}, suggesting a change in the interaction mode of the phthalocyanine molecules with each other. A more disorganized structure tends to prevent the stacking of the phthalocyanine molecules and their mechanical coupling through the H-aromatic out-of-plane bending vibrational mode, thus splitting the FT-IR vibrational mode.

Wide-Angle X-ray Scattering (WAXS). WAXS analysis was carried out with the M_aOcPc's and each of the M_aOcPc-

https://doi.org/10.1021/acsaem.4c02297
ACS Appl. Energy Mater. XXXX, XXX, XXX−XXX

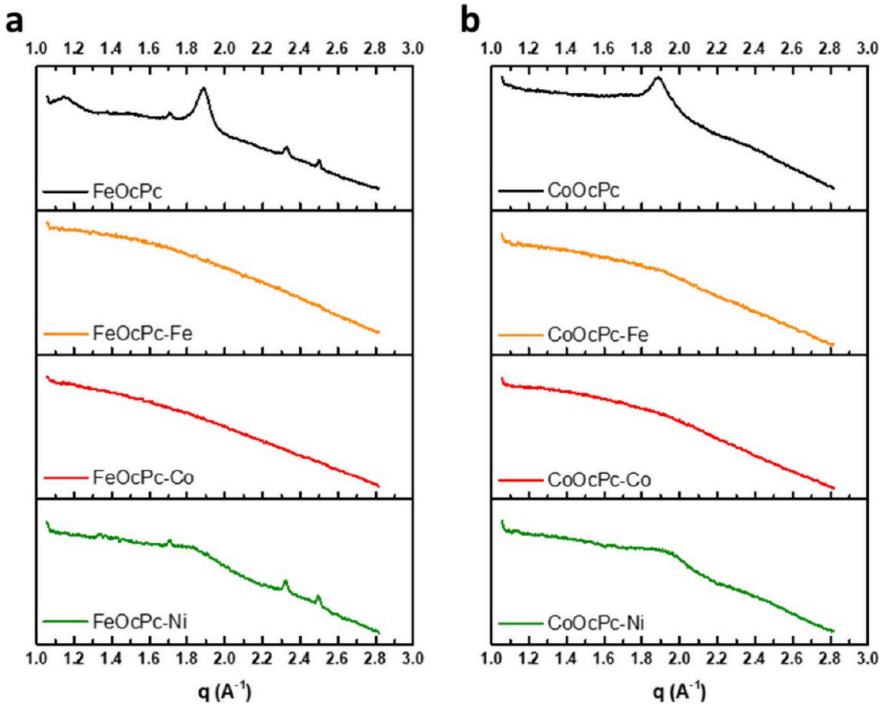

Figure 2. Comparative WAXS plots of (a) FeOcPc, FeOcPc-Fe, FeOcPc-Co, and FeOcPc-Ni and (b) CoOcPc, CoOcPc-Fe, CoOcPc-Co, and CoOcPc-Ni.

M_b CP materials (Figure 2), and the results were qualitatively analyzed to evaluate the possible formation of amorphous CPs.

The WAXS curves of FeOcPc and CoOcPc (Figure 2) exhibit a well-defined peak of q value near 1.9 A^{-1} that can be attributed to stacking of Pc molecules. Nevertheless, this feature disappeared in M_aOcPc-M_b CP materials, as suggested by the complete absence of the 1.9 A^{-1} peak in the WAXS curves of FeOcPc-Fe and FeOcPc-Co (Figure 2a), as well as of CoOcPc-Fe and CoOcPc-Co (Figure 2b), indicating a much higher degree of disorganization. However, the FeOcPc-Ni and CoOcPc-Ni materials exhibited a broad peak at 1.8−1.9 $Å^{-1}$, indicating that these CPs have structural organization intermediary between that of M_aOcPc's and M_aOcPc-M_b materials, with some degree of π-stacking of the phthalocyanine molecules. The quite high degree of structural disorder indicated by WAXS analysis corroborates the hypothesis of formation of CPs with amorphous character but some H-type structures, as indicated by the appearance of an out-of-plane bending mode coupling the aromatic macrocyclic rings in the FT-IR spectrum.

The structure of the CP materials induced by the formation of the bridging peripheral metal carboxylate complexes should define the relative amount of inner M_a and peripheral M_b ions, or in other words the stoichiometry of M_aOcPc and M_b ions. Accordingly, the percentage amounts of peripherally coordinated metal ions (Fe, Co or Ni) and phthalocyanine inner ring metal ion (Fe or Co) were determined by EDX analysis, and the M_b/M_a values are presented in Table 2. Here it is important to emphasize that the EDX technique cannot distinguish the chemical environment or the oxidation state of a metal ion, such that the M_b/M_a ratio can be determined only if M_a and M_b are distinct elements but not when they are the same, such as in FeOcPc-Fe and CoOcPc-Co.

In the ideal situation of formation of a CP material with well-defined composition and structure in which each metal ion is bound to a pair of vicinal carboxylate groups of two distinct M_aOcPc bridging ligands forming a layered grid-like structure, the M_b/M_a value should be close to 2. However, the M_b/M_a ratio tend to be slightly larger than 2, indicating an excess of peripheral M_b ions. Interestingly, this result contrasts with the FT-IR result, indicating that all vicinal COO^- are bound to a metal ion in bidentate mode. This suggests that the second carboxylate group in a vicinal pair must be interacting with another cation, such as K^+, or a proton, H^+, in a similar way. In fact, relatively large amounts of this alkali metal cation were found in the EDX analysis, as shown in Table 2, confirming the hypothesis of a metal carboxylate complex as nodes of M_aOcPc-M_b grid-type CPs. Schematic representations of the M_aOcPc-M_b grid-type materials and their Pc monomers are presented in Scheme 3. It is important to highlight that, despite the schematic representation of Pc sheets, the material does not present a defined structure. Therefore, it is amorphous, as shown by WAXS analyses (Figure 2) and Scheme 3.

Table 2. Relative Percentages of Metal Ions in M_aOcPc-M_b CP Materials

	Relative metal quantity (%)			
M_aOcPc-M_b	Fe	Co	Ni	M_b/M_a
FeOcPc-Fe	94.03	–	–	–
FeOcPc-Co	30.89	63.24		2.05
FeOcPc-Ni	27.27	–	69.09	2.53
CoOcPc-Fe	57.95	21.86		2.65
CoOcPc-Co	–	91.53	–	–
CoOcPc-Ni	–	25.87	66.23	2.56

Cyclic Voltammetry and the General Electrochemical Behavior of the M_aOcPc-M_b CPs. In a recent work, Costentin showed that proton-coupled electron transfer (PCET) of the OER can present distinct voltammetric profiles

https://doi.org/10.1021/acsaem.4c02297
ACS Appl. Energy Mater. XXXX, XXX, XXX−XXX

Scheme 3. Schematic Representation of the Co Octacarboxyphthalocyanine (CoOcPc), Fe Octacarboxyphthalocyanine, and the Generic $M_aOcPc\text{-}M_b$ Polymer Grid

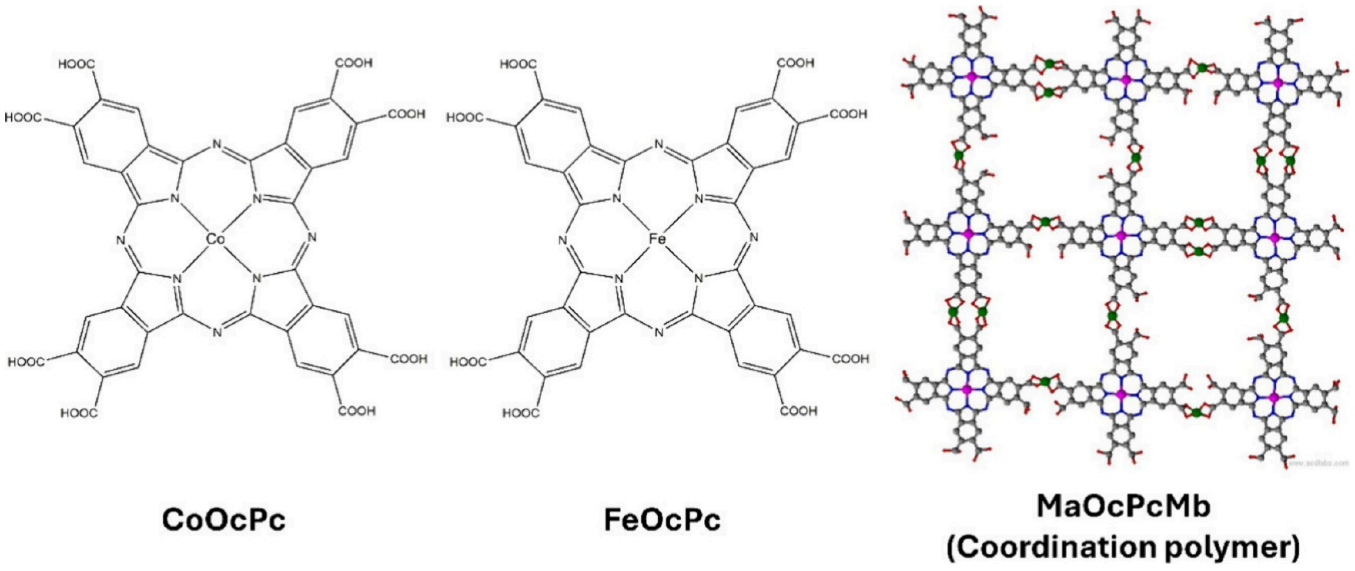

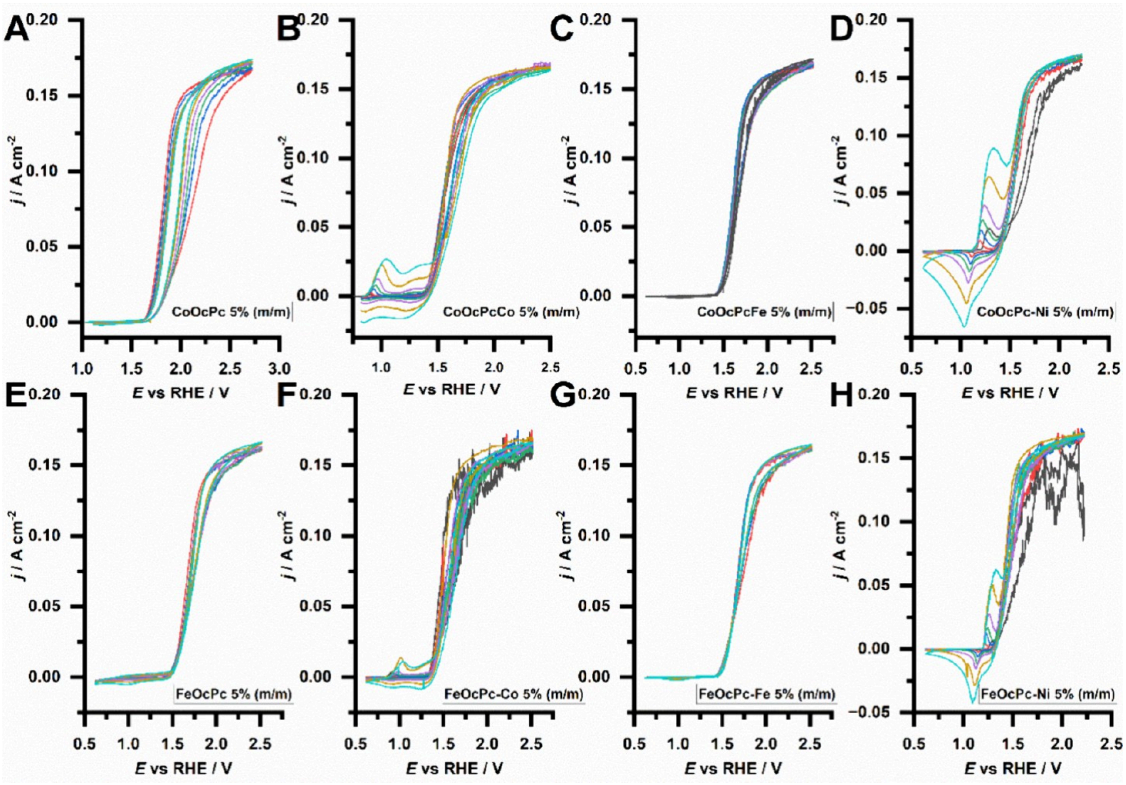

Figure 3. CVs obtained with (A) CoOcPc, (B) CoOcPc-Co, (C) CoOcPc-Fe, (D) CoOcPc-Ni, (E) FeOcPc, (F) FeOcPc-Co, (G) FeOcPc-Fe, and (H) FeOcPc-Ni in 0.85 mol L^{-1} KOH solution (pH = 13.8), at distinct potential scan rates, indicated by different colored lines: gray, 0.010 V s^{-1}; red, 0.020 V s^{-1}; blue, 0.050 V s^{-1}; green, 0.100 V s^{-1}; purple, 0.200 V s^{-1}; dark yellow, 0.500 V s^{-1}; and cyan, 1.000 V s^{-1}.

(sigmoidal or peak-shaped), depending on their limiting step and the presence or absence of a buffer solution. In the presence of the buffer, a peak shape tends to be observed, while in its absence, a sigmoidal profile is usually expected.[45]

To evaluate the electrochemical behavior and mechanism of the $M_aOcPc\text{-}M_b$ CPs as OER catalysts, the cyclic voltammograms of each material in aqueous medium, Figure 3, were analyzed. First, all materials presented a sigmoidal voltammetric profile at potentials more positive than about 1.2 V vs RHE, which strongly indicates that all studied materials present some catalytic activity toward the OER.[45] Second, the occurrence of a catalytic process is endorsed by the strong flux of bubbles from the working electrode, especially at slower scan rates. Third, it was also noticed that the voltammograms exhibited similar voltametric profiles with a well-defined plateau and limiting current at all scan rates, a result that strongly indicates that the process presents a pseudo-zero-order kinetics rate. In other words, the plateau current (I_{pl}) is

https://doi.org/10.1021/acsaem.4c02297
ACS Appl. Energy Mater. XXXX, XXX, XXX−XXX

Table 3. OER Half-Wave Potentials for the $M_aOcPc\text{-}M_b$ CP Materials (Error of ±0.002 V)

	$E_{1/2}$ (V vs RHE)							
Scan rate (V s^{-1})	CoOcPc (V)	CoOcPc-Co (V)	CoOcPc-Fe (V)	CoOcPc-Ni (V)	FeOcPc (V)	FeOcPc-Co (V)	FeOcPc-Fe (V)	FeOcPc-Ni (V)
0.01	1.584	1.344	1.405	–	1.466	1.316	1.453	1.325
0.02	1.584	1.353	1.401	1.342	1.470	1.315	1.453	1.289
0.05	1.605	1.359	1.387	1.339	1.483	1.348	1.437	1.305
0.10	1.600	1.379	1.401	1.362	1.473	1.354	1.440	1.311
0.20	1.602	1.391	1.404	1.383	1.482	1.361	1.447	1.328
0.50	1.603	1.424	1.413	1.431	1.495	1.374	1.448	1.360
1.00	1.603	1.472	1.425	1.468	1.500	1.399	1.449	1.400

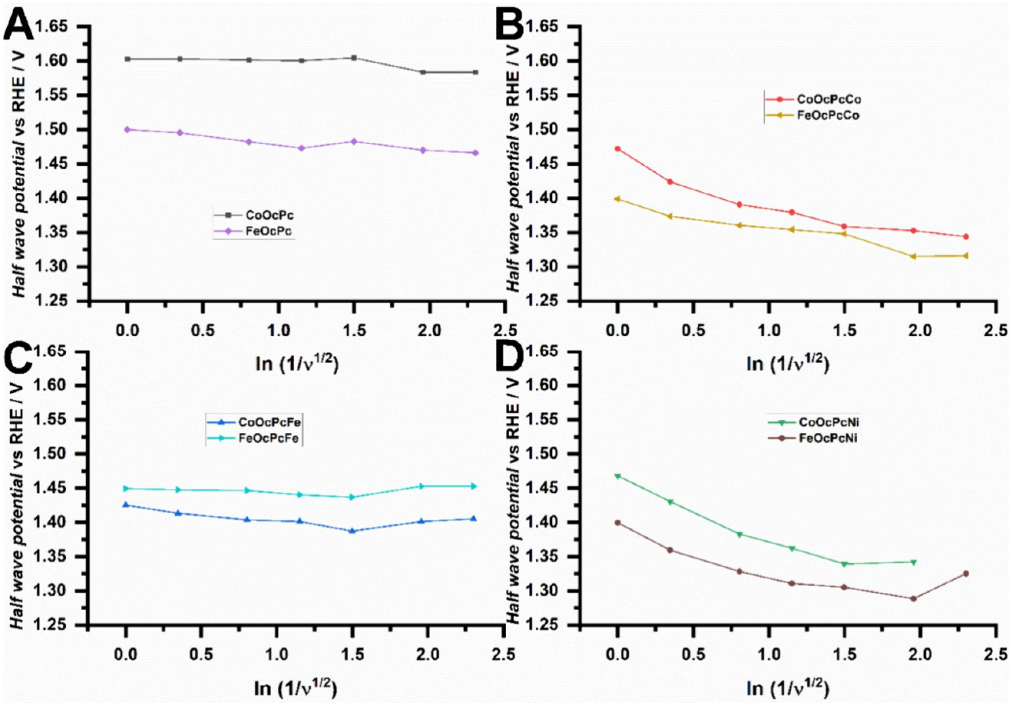

Figure 4. Half-wave potential as a function of the natural logarithm of the reciprocal of the square root of the scan rate ($\ln(1/v^{1/2})$) plots for (A) M_aOcPc, (B) $M_aOcPc\text{-}Co$, (C) $M_aOcPc\text{-}Fe$, and (D) $M_aOcPc\text{-}Ni$.

not limited by the amount of substrate reaching, or available at, the electrode surface. The figure also shows a hysteresis effect in all CVs that can be correlated to the adsorption strength of the substrate and/or the process intermediates onto each material. Hereby, it is related to a change in the electrode's surface. For instance, a change in the $M_aOcPc\text{-}M_b$ materials' active site can generate hysteresis. As long as they are under the OER conditions, the Pc's generally present an oxygen or hydroxy bound to the axial positions of the coordinated metal ion. The hysteresis implies the conversion of the hydroxyl to an oxo ligand, passing through a peroxide intermediate during the process, according to the mechanism presented in Table 1.[12,36] This result also shows that, in these cases, the potential imposed by the scan rate pushes forward the electrode kinetics, and the material does not hastily reset the catalytic cycle, thus jeopardizing the occurrence of the OER. In short, our materials exhibit a counterintuitive outcome, more specifically a faster turnover and less hysteresis as a function of the scan rate.

In addition, it is also important to notice that two quasi-reversible pre-peaks were observed for the $M_aOcPc\text{-}Co$- and $M_aOcPc\text{-}Ni$-modified CPEs, which according to the literature can be observed only when an electrochemical process alternates with a coupled chemical reaction in an ECEC mechanism, which presents a process that has a E^0_{cat} and E^0_f difference larger than 0.3 V ($\Delta E > |E^0_{cat} - E^0_f|$).[46,47] In our case, the peripheral metal complexes of the CPs present an E^0_{cat} that differs from the E^0_f of the M_aOcPc responsible for the activation of those electrocatalytic sites. In this context, the $E_{1/2}$ potential of the OER can also provide relevant information on the electrocatalytic performance of the material. Moreover, these processes are also attributed to the formation of the oxide/hydroxide derivatives of the coordinated metal ions.

Overall, despite the similar S-shaped profile obtained for all materials studied, the curves present different inclinations, and hence they have distinct kinetic efficiencies toward OER. LSVs in Figure S2 are presented according to the way traditionally used in materials and catalysis works.

To further explore the differences of each catalyst's performance, the $E_{1/2}$ potentials and electrode kinetics were better explored by analyzing the potential itself and how the current associated with the OER process increases next to the $E_{1/2}$ potential ("the kinetic region") as a function of the scan rate.

Half-Wave Potentials ($E_{1/2}$) and Thermodynamic Analysis. Usually, onset potentials are a traditional way to

https://doi.org/10.1021/acsaem.4c02297
ACS Appl. Energy Mater. XXXX, XXX, XXX−XXX

Table 4. Charge-Transfer Coefficients (β) of the $M_aOcPc\text{-}M_b$ Coordination Polymers, Considering Them as OER Electrocatalysts

	β							
Scan rate ($V\ s^{-1}$)	CoOcPc	CoOcPc-Co	CoOcPc-Fe	CoOcPc-Ni	FeOcPc	FeOcPc-Co	FeOcPc-Fe	FeOcPc-Ni
0.01	0.868	0.235	0.414	0.199	0.572	0.915	0.791	0.532
0.02	0.868	0.263	0.329	0.643	0.627	1.239	0.793	0.964
0.05	0.729	0.289	0.327	0.529	0.576	0.969	0.812	0.92
0.10	0.641	0.308	0.323	0.412	0.557	0.703	0.792	0.621
0.20	0.590	0.296	0.367	0.294	0.542	0.648	0.760	0.475
0.50	0.529	0.257	0.418	0.164	0.468	0.521	0.689	0.311
1.00	0.469	0.203	0.436	0.121	0.396	0.302	0.638	0.193

study catalytic processes. Despite that, the literature is reticent in using this parameter to describe the process,[48] especially in gas evolution reactions since the interface will be covered up with microbubbles and, consequently, the measured potential tend to be inaccurate. To solve this issue, the half-wave potentials were obtained and used to describe the electrocatalytic mechanism, even though the onset potential was evaluated in the LSV, presented in Figure S2.

Observing Table 3 and Figure 4, the behavior of the electrodes can be paired according to the M_b of the material. Figure 4A,C shows that the half-wave potentials remain constant as a function of the natural logarithm of inverse of the square root of the scan rate ($\ln(1/v^{1/2})$), while in Figure 4B,D a decreasing slope can be observed. Despite the pairing of the materials as a function of M_b, it is important to notice that, in electrochemistry, a constant potential as a function of the scan rate indicates a quite high standard electron transfer rate constant, considering that a potential shift indicates a diminished value, hence a quasi-reversible or irreversible process. Thereby, the results do suggest the MPc's and the CPs with Fe as the bridging metal ion should present the best turnover values. However, these materials presented the worst turnovers among all materials (a result that will be explored in another section), implying the reaction involves chemical steps, such as adsorption and desorption, not only the electron-transfer process.

The iron-poor catalytic activity of the CPs' bridging sites can be explained as a direct effect of Sabatier's principle. According to the literature, one of the main features of OER is the competition of the dimerization process of two nearby oxyl groups and their further oxidation into peroxyl groups.[12] For both of these processes to take place, it is required that a higher (or exotic) oxidation state catalytic site must be formed, most likely in a tetravalent state. In this particular case, the Ni^{IV}, Co^{IV}, and Fe^{IV} ions present the d^0, d^5, and d^4 electronic configurations, respectively, which are stabilized by a decreasing ligand field energy. Accordingly, the activation barrier for generation of Ni^{IV} tends to be lower than for Co^{IV}, and this tends to be lower than for Fe^{IV}, and their binding energies tend to decrease in the same order. This is a textbook example of Sabatier's principle, where a higher energy activated complex leads to a slower kinetics and, thus, to a lower turnover number.

In addition, the mechanistic hinged catalysis is a direct effect of the distorted square planar M_a sites of the phthalocyanines, which tend to favor the formation of Fe^{IV}═O and Co^{IV}═O species due to the basicity of the deprotonated ligand and delocalization of charge density into the sp^2 π-system of the macrocyclic ring. Accordingly, the formation of this more stable intermediate state can induce electronic effects that can jeopardize the kinetics of the OER due to the additional energy required to overcome the next electrochemical step responsible for the formation of the activated complex.

To further evaluate the kinetics of the systems, the Tafel analysis was performed, as detailed below.

Kinetics Evaluation by Tafel Analysis. Complementarily to the half-wave potential analysis, the kinetics of the OER process of each material was evaluated considering the corresponding charge-transfer coefficients (β), which reflect the position of the transition state in the reaction coordinates. According to Hammond,[49] the structure of the transition state can be similar to that of the reagents, or the products, and its thermodynamic and activation properties define the RDS and mechanism of the reaction. An analysis of the transition state can show how the reorganization energy influences the activation energy and the $\Delta G^{\ddagger}$ of the electrocatalytic reaction for each material.[50]

The β values were determined based on eqs 2, 3, 4, and 5.[50−52] The data obtained from the traditional Tafel analysis, eq 3, and mass-corrected Tafel analysis, eq 4, were then plotted as a function of the scan rate. This allowed us to calculate that kinetic parameter as a function of the variation of the potential scan rate, since its value is directly related to the ratio of activation energy and reorganization energy λ of the rate-determining charge-transfer process, according to eq 6.[53]

$$\ln I_p = \ln FAk^0[A]_0 + \frac{\beta F}{RT}(E - E_f^0) \tag{2}$$

$$\beta(E) = \frac{F}{RT}\frac{d\ln I}{dE} \tag{3}$$

$$\beta(E) = \frac{F}{RT}\frac{d\left|\ln\left(\frac{1}{I}\right) - \left(\frac{i}{I_{lim}}\right)\right|}{dE} \tag{4}$$

$$\beta = n' + \beta_{RDS} \tag{5}$$

$$\beta = \frac{1}{2}\left(1 + \frac{\Delta G^{\ddagger}}{\lambda}\right) \tag{6}$$

Here, I_p is the peak current, F the Faraday constant in C mol^{-1}, A the electrode area in cm^2, k^0 the standard rate constant in cm s^{-1}, $[A]_0$ the concentration of the analyte in the bulk in mol cm^{-3}, E the applied potential in V, E_f^0 the formal redox potential of the substrate in V, R the gas constant in J K^{-1} mol^{-1}, T the absolute temperature in K, I the current in amperes, β the adimensional oxidation charge-transfer coefficient, β_{RDS} the adimensional oxidation charge-transfer coefficient at the RDS, $\Delta G^{\ddagger}$ the Gibbs activation energy in kJ mol^{-1}, and λ the reorganization energy in mol kJ^{-1}.[54]

https://doi.org/10.1021/acsaem.4c02297
ACS Appl. Energy Mater. XXXX, XXX, XXX−XXX

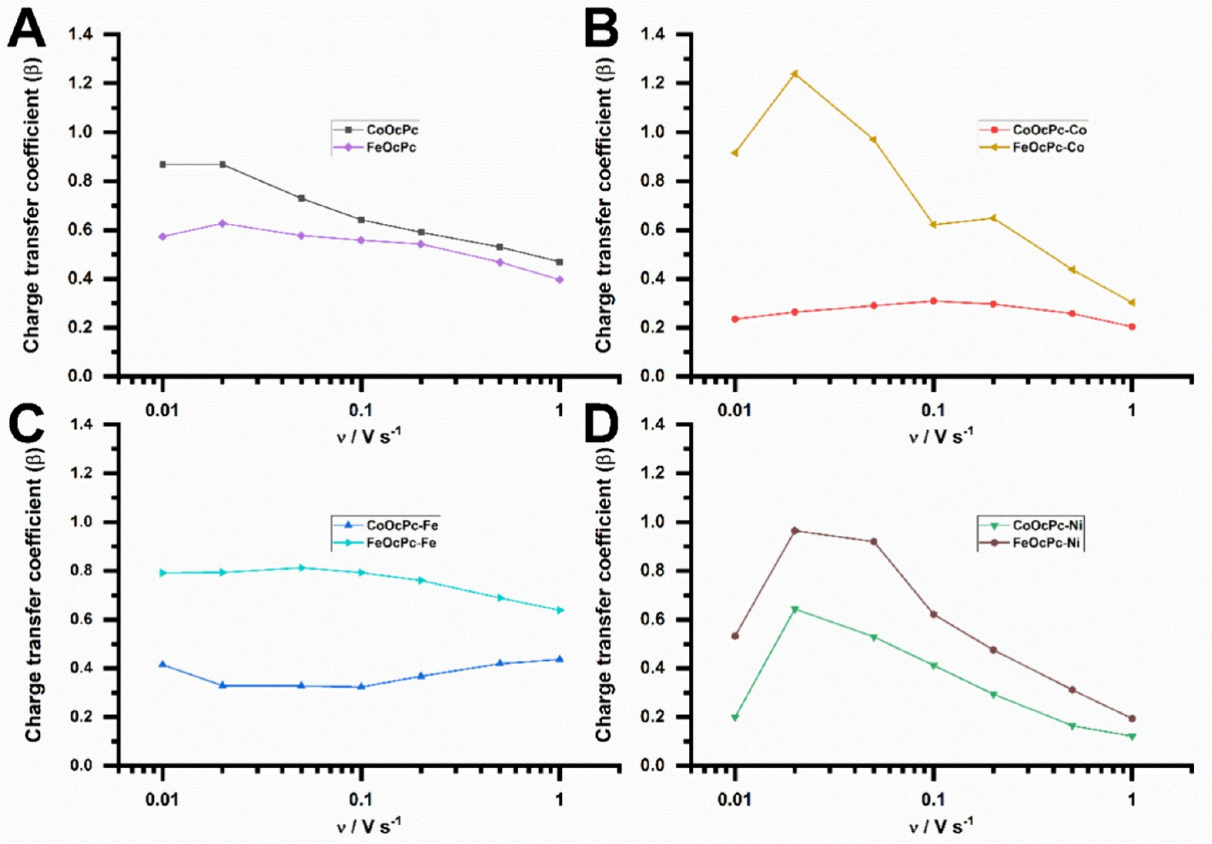

Figure 5. Charge-transfer coefficients (β) as a function of the scan rate: (A) M_aOcPc, (B) M_aOcPc-Co, (C) M_aOcPc-Fe, and (D) M_aOcPc-Ni.

Table 4 and Figure 5 show the charge-transfer coefficients (β) of each material as a function of the scan rate. Generally, the β values are in the 0 to 1 range, thus suggesting that the RDS can be directly associated with the first electrochemical step of the reaction mechanism. It also is in agreement with the CVs results, Figure 3, whereas the hysteresis decreases overall with the increase of the scan rate, suggesting that a large adsorption does occur and not all the adsorbed substrate is converted. The increase of the scan rate increases the electrode kinetics, consuming the adsorbed substrate and consequently diminishing the hysteresis observed. Therefore, the hysteresis is directly associated with the adsorption of H_2O molecules and/or OH^- ions onto the catalyst[9] and the intermediate formation which agrees with the Sabatier principle.[55]

Figure 5 shows that, excluding M_b = Co, the β values present a mechanistic correlation between the charge-transfer coefficients and the M_b of the CPs. In addition, this result suggests that the catalysts show a narrow range of efficiency in terms of the scan rate (flux). Competition will occur, as the process depends on the capacity of the material to adsorb onto the substrate and later on its capability to regenerate the catalyst throughout the OER. Any imbalance in this process leads to a decrease of the OER efficiency. Hereby, the competition of the RDSs involving those mechanisms results in the traditional "volcano plot" of catalytic efficiency—once again, a result consistent with the Sabatier principle of catalysis.[55] The traditional Tafel plots were also obtained and are presented for comparison in Figure S3.

Compiling the half-wave potentials and Tafel analysis results, CV normalization ($\frac{I}{FA\Gamma^0 kC} \times E$) was performed to observe the mechanistic criteria of the electrocatalytic reaction, in which the k values were obtained via foot of the wave analysis (FOWA),[56] Figures S4 and S5.

In this type of electrocatalytic system, the water acts as a Lewis base, even though the hydroxyl concentration is elevated (pH = 14), since water molecules are approximately 56 times more abundant than the hydroxide ions. In this case, two dimensionless parameters govern the processes, $\lambda_{S,bh}$ and λ_{-bh}, which can be calculated based on eqs 7 and 8, respectively,[45]

$$\lambda_{S,bh} = kC_S^0/k_{bh}C_b \tag{7}$$

$$\lambda_{-bh} = k_{-bh}\Gamma^0 \Big/ \sqrt{\frac{D_0 F\nu}{RT}} \tag{8}$$

where k is the apparent rate constant in cm^{-1}, C_S^0 is the surface concentration of the substrate in mol cm^{-3}, k_{bh} is the deprotonation rate constant in cm^{-1}, C_b is the base concentration in mol cm^{-3}, k_{-bh} is the reprotonation rate constant in cm^{-1}, Γ^0 is the catalyst surface coverage in C, D_0 is the diffusion coefficient of the proton in cm s^{-1}, F is the Faraday constant, ν is the scan rate in V s^{-1}, R is the gas constant in J mol^{-1} K^{-1}, and T is the temperature in K.

The first term ($\lambda_{S,bh}$) is correlated to the competition of the substrate oxidation and the proton-transfer steps as the RDS step, which occur irreversibly in proton transfers. The second term (λ_{-bh}) is related to the competition of the reinsertion of the proton into the process ("reprotonation") and its diffusion away from the electrode interface.

Analyzing the system, the parameter $\lambda_{S,bh}$ should be very small while k_{bh} is a very large value, due to the alkali pH. Therefore, its logarithm (log $\lambda_{S,bh}$) should be negative. Moreover, the logarithm of λ_{-bh} (log λ_{-bh}) is most likely

https://doi.org/10.1021/acsaem.4c02297
ACS Appl. Energy Mater. XXXX, XXX, XXX−XXX

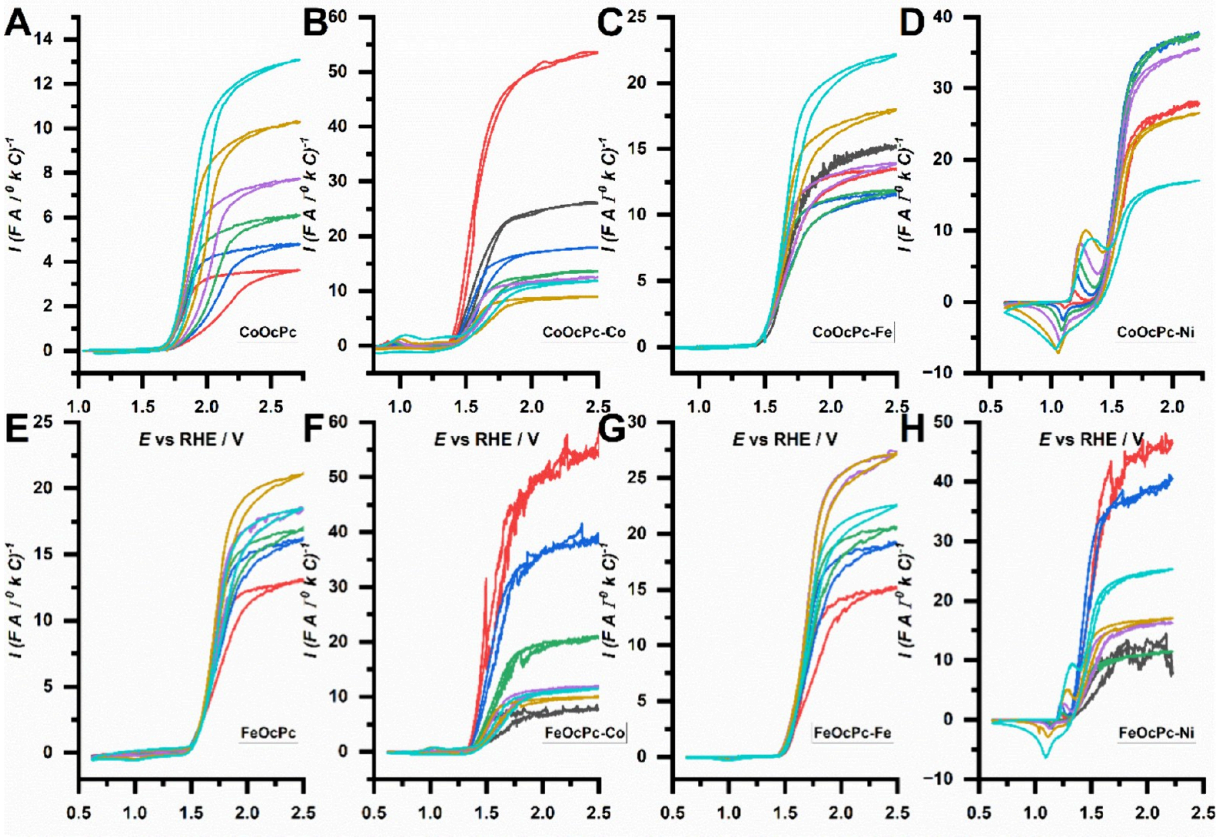

Figure 6. Dimensionless CV: voltammograms with (A) CoOcPc, (B) CoOcPc-Co, (C) CoOcPc-Fe, (D) CoOcPc-Ni, (E) FeOcPc, (F) FeOcPc-Co, (G) FeOcPc-Fe, and (H) FeOcPc-Ni in 0.85 mol L^{-1} KOH solution (pH = 13.8) at distinct potential scan rates to evaluate a PTET pathway in a nonbuffered medium (water as a Lewis base): gray, 0.010 V s^{-1}; red, 0.020 V s^{-1}; blue, 0.050 V s^{-1}; green, 0.100 V s^{-1}; purple, 0.200 V s^{-1}; dark yellow, 0.500 V s^{-1}; cyan, 1.000 V s^{-1}.

found between −1 and 1 ($1 < \lambda_{-bh} < 1$). Figure 6 shows dimensionless voltammograms at distinct scan rates. All materials presented S-shaped normalized voltammograms that appear to cascade, although not all of them in the exact order of the scan rates. In addition, the $E_{1/2}$ values do not appear to significantly shift, remaining practically constant, and finally, all voltammograms kept a sigmoidal shape and presented no tendency to form peaks. Correlating this data with Figure 3, where all the voltammograms present the same plateau current, independent of the scan rate, it is possible to infer that these results are in full agreement with the PTET pathway with water as a proton acceptor.[45] Merging this information with the log $\lambda_{S,bh}$ and log λ_{-bh} values provides the conclusion of an irreversible proton transfer followed by the oxidation of the substrate as the RDS ($PT_{irrev}SO_{RDS}$), whose behavior is illustrated in Scheme 4. Moreover, the sequence of OERs will be "locked" by the strong alkalinity, and therefore in agreement with the observed voltammograms and Scheme 5, which shows that despite the variations of $\frac{\Gamma^0}{\nu}$ the limiting step does not shift from $PT_{irrev}SO_{RDS}$, Scheme 4. Combining the data from Schemes 4 and 5, the generic mechanism is presented in Scheme 6.

A compilation and in-depth analysis of the experimental data and mechanistic information (Scheme 5), made possible by proposing the main steps of the general OER catalytic mechanism by $M_aOcPc\text{-}M_b$, is shown in Scheme 6.

To characterize the mass transport processes in the electrocatalytic reaction and obtain further information regarding the electrode surface dynamics, electrochemical impedance spectroscopy analyses were performed.

Scheme 4. Representation of the Zone Diagram for a PTET Catalytic Pathway in Unbuffered Systems[a]

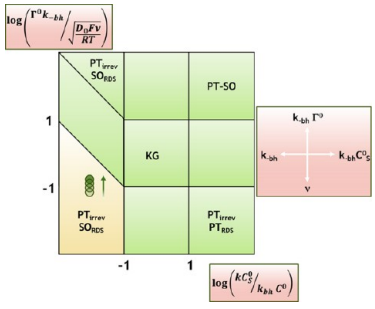

[a]KG is a general case, PT_{rev} is a reversible proton transfer, PT_{irrev} is an irreversible proton transfer, RDS stands for the rate-determining step, SO is a substrate oxidation, and PT-SO is a mixed controlled region.

Interface Characterization and Evaluation of OER Catalytic Mechanisms by Electrochemical Impedance Spectroscopy (EIS). Based on the voltammetric results obtained for the OER and to better comprehend the modified electrode behavior, especially the influence of the CPE material and electrolyte solution, a careful EIS study was performed with the $M_aOcPc\text{-}M_b$ CPs at potentials before and after the half-wave potential of the OER. This section aims to evaluate

https://doi.org/10.1021/acsaem.4c02297
ACS Appl. Energy Mater. XXXX, XXX, XXX−XXX

Scheme 5. General OER Catalytic Reaction Depicting the Possibilities of Reaction Pathways as a Function of pH

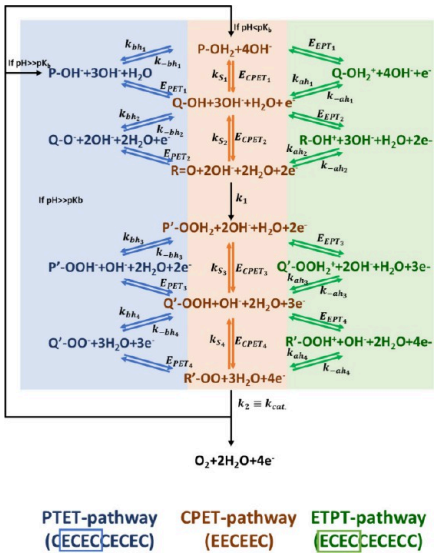

Scheme 6. General OER Catalysis Mechanism Performed by the M_aOcPc-M_b CPs

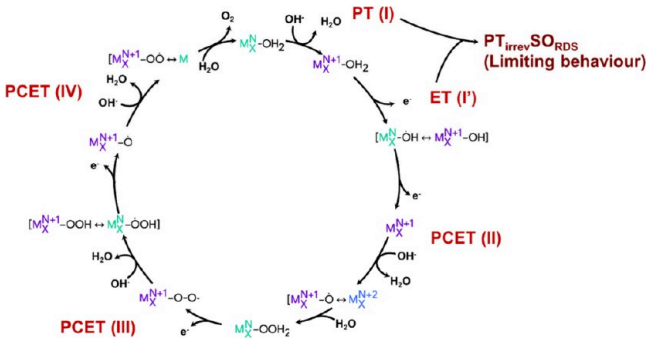

the uncommon Nyquist plot result of such an electrocatalytic process.

Figure 7 shows the Nyquist -Z″ vs Z′ plot for the CP materials and the theoretical equivalent circuits which fit the experimentally obtained profile. At the beginning, a great difference in the values can be observed, depending on the applied potential and its position in the catalytic wave. At this point, it is important to emphasize that a high-impedance semi-arch is observed for all materials with an applied potential below the OER half-wave potential. Nevertheless, once the applied potential reaches the necessary electrochemical potential to activate the CP, a significant diminishment of the Rct (Charge Transfer Resistence) in Ω. can be observed, as an expressive reduction of the semi-circle radius associated with the respective activated electron-transfer process. Moreover, activation of the CP not only leads to a reduction in the semi-arch but also allows the observation of the OER performance in two distinct situations. First, when the E_{app} is below the reaction half-wave potentials (Figure 7E,H), the diffusion region is observed for some materials as 45° parallel lines at low frequencies, which is characteristic of an electrode process limited by semi-linear infinite diffusion mass transport. In contrast, a large opened semi-arch can be observed in the other case (Figure 7A−D,F, and G), indicating a process governed by a finite length diffusion. This uncommon behavior is usually observed in electrocatalytic processes[57] in which the mass transport occurs in a partially blocked electrode surface with some specific points (active sites) performing the heterogeneous electron transfer, thus resulting in an S-shaped voltammogram.

Second, for all materials, when the E_{app} is above the $E_{1/2}$ potential, the diffusion contribution changes to a finite length diffusion process (finite length Warburg, FLW, or Warburg short, W_S).[58] In other words, an efficient diffusion process is provided by the partially blocked surface that can be associated with the thin oxygen bubble layer generated by the OER,[59] as corroborated by the phase angle tending to 0° in the low-frequency range. The reduction of the W_S impedance upon activation evinces this combination of a partially blocked surface and the thin bubble layer resulting in a more efficient diffusion, suggesting that a more intense microconvection phenomenon is promoted by evolution of the oxygen gas bubbles. This shows analogy with the microconvection promoted by mercury droplets in polarography, thus limiting the expansion of the diffusion layer.[60] This observation is corroborated by the CV profiles that show lower hysteresis for the OER after activation of the CPE, which indicates a more efficient mass transport of the electroactive species to the electrode surface. The validation of the EIS data with the equivalent circuits is also presented in Figure 7, whilst the EIS performed with other E_{app}, are presented in Figure S1.

Since the catalysts present the same plateau current and similar reaction mechanisms but distinct Nyquist plots, the turnover frequencies of each of them performing the OER were evaluated.

Foot of the Wave Analysis (FOWA) and Turnover Frequency (TOF). TOF analysis, also known as a catalytic Tafel plot, allows us to determine the time required to execute a full catalytic reaction cycle regenerating the electrocatalyst. According to Costentin and Savéant,[47] the TOF is defined as "the ratio of the number of molecules transformed by the number of catalyst molecules effectively used in the transformation per unit of time", as described by eq 9,[47]

$$\mathrm{TOF} = \frac{N_{prod}}{N_{active\ cat}} = \frac{2k_{cat(app)}[A]_0}{1 + e^{[-\frac{F}{RT}(\eta)]}\, e^{[\frac{F}{RT}(E^0_{f(cat)} - E^0_{f(OER))}]}} \quad (9)$$

with $\mathrm{TOF}_{max} = k_{cat(app)}[A]_0$, where $[A]_0$ is the concentration of substrate in mol dm^{-3}, $k_{cat(app)}$ is the apparent catalytic rate constant in s^{-1}, $\eta = (E^0_{f(OER)} - E_{app})$ in V is the overpotential, and $E^0_{f(cat)}$ is the formal redox potential of the catalyzed reaction in V. Nevertheless, for the purpose of TOF analysis, the $k_{cat(app)}$ values must be determined by the FOWA. The TOF_{max} is provided by the I_0 (plateau current) for conversion of A, as described by eq 10:

$$\frac{i_0}{FA} = 0.446[A]_{bulk}\sqrt{D_{0(A)}}\sqrt{\frac{RT}{F\vartheta}2k_{cat(app)}[Cat]_{sup}} \quad (10)$$

In the Tafel analysis, the TOF focuses the attention on the initial part of the faradaic process in the voltammogram, also known as the Tafel region, where the concentration of the analyte is virtually the same as in the bulk and the heterogeneous electron-transfer process is uniquely limited by the charge-transfer kinetics.[61]

Analogously, the unperturbed current of the system can be obtained from the very beginning of the faradaic curve, as described by eq 11.

https://doi.org/10.1021/acsaem.4c02297
ACS Appl. Energy Mater. XXXX, XXX, XXX−XXX

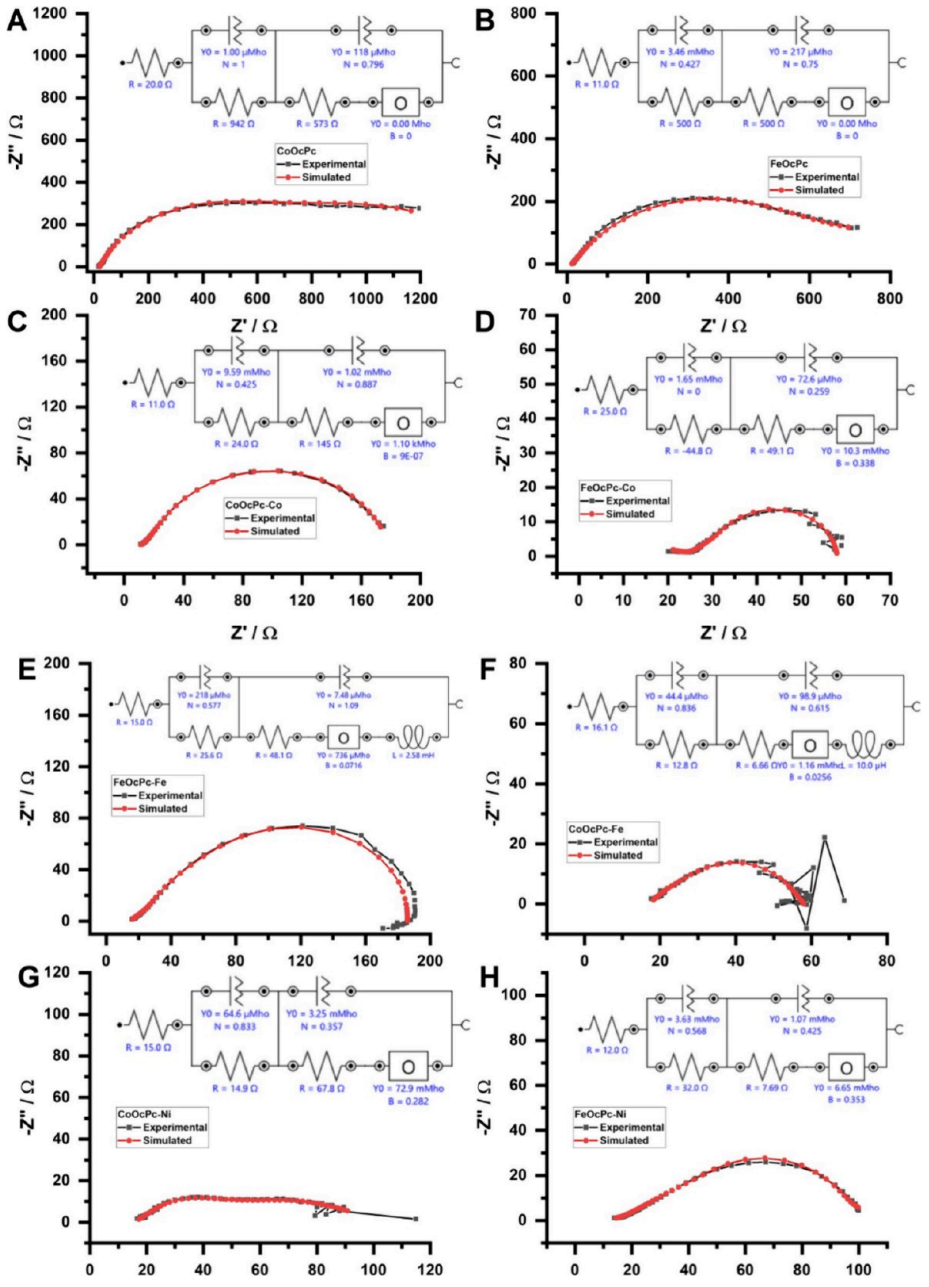

Figure 7. Experimental and theoretical Nyquist plots at distinct applied potentials generated based on the equivalent circuit parameters, fitting the EIS data of the CPE loaded with the M_aOcPcM_b materials: (A) CoOcPc, (B) CoOcPc-Co, (C) CoOcPc-Fe, (D) CoOcPc-Ni, (E) FeOcPc, (F) FeOcPc-Co, (G) FeOcPc-Fe, and (H) FeOcPc-Ni. E_{app} values are shown with and without the catalytic process, frequencies between 0.1 and 10^6 Hz, and the respective equivalent circuits.

$$\frac{i}{FA} = \frac{[A]_0 \sqrt{D_{0(A)}} \sqrt{2k_{cat(app)}[Cat]_{sup}}}{1 + e^{[\frac{F}{RT}(E_{app} - E^0_{f(OER)})]}} \quad (11)$$

In addition, eqs 8 and 9 can be combined into eq 12, thus allowing us the determination of the $k_{cat(app)}$ values listed in Table 3 from the slope of the $\frac{i}{i_0} \times (1/(1/(1 + e^{[\frac{F}{RT}(E_{app} - E^0_{f(OER)})]})$:[61,62]

$$\frac{i}{i_0} = \frac{2.24\sqrt{\frac{RT}{F\vartheta}2k_{cat(app)}[Cat]_{sup}}}{1 + e^{[\frac{F}{RT}(E_{app} - E^0_{f(OER)})]}} \quad (12)$$

The FOWA analysis, Figures S4 and S5, endorses the competition of the two mechanisms previously discussed, as all the electrocatalytic materials present a dependence of the scan rate in the plots of I/I_0 as a function of $1 + \exp[F/RT(E_{app} - E^0_f - E^0_{f(OER)})]$.

The apparent catalytic constant, $k_{(cat)app}$, was determined based on the FOWA, Figures S4 and S5, the formal potential of the catalyst (E^0_{cat}) was obtained from the CVs, and the concentration of the catalyst in the electrode surface was determined by integration of the pre-peaks and extrapolated to all of them, as the amount of material used in each CPE was exactly the same. These values are compiled in Table 5.

The catalytic Tafel plots (log TOF vs η) and the TOF analysis can be carried out using the data presented in Table 3.

https://doi.org/10.1021/acsaem.4c02297
ACS Appl. Energy Mater. XXXX, XXX, XXX−XXX

Table 5. Formal Potential (V) and the Respective Apparent Catalytic OER Rate Constants (s^{-1}) of the CP Materials, and the Surface Concentration of Catalyst (mol cm^{-2}), Estimated from the FOWA Presented in Figures S4 and S5 (Electrode Area = 0.041 cm^2)

Catalyst	E^0_{cat} vs RHE (V)	$k_{cat(app)}{}_1$ ($\times 10^5$ s^{-1})	$[Cat]_{sup}$ ($\times 10^{-7}$ mol cm^{-2})
CoOcPc	0.80	1.07	2.15
CoOcPc-Co	0.75	1.06	2.15
CoOcPc-Fe	0.78	1.08	2.15
CoOcPc-Ni	0.72	1.11	2.15
FeOcPc	0.85	1.03	2.15
FeOcPc-Co	0.65	1.04	2.15
FeOcPc-Fe	0.85	1.03	2.15
FeOcPc-Ni	0.60	1.10	2.15

The analyses were performed using the voltammograms at 0.01 V s^{-1} since, in general, this was the best catalytic condition determined for all of the catalytic materials, Pc's and CPs. Figure 8A shows the comparison of the materials' performance toward the OER.[56] Considering both thermodynamic and kinetic analyses, the catalytic performance followed the same sequence, **FeOcPc-Ni > FeOcPc-Co > CoOcPc-Ni > CoOcPc-Co > CoOcPc-Fe > CoOcPc > FeOcPc ≈ FeOcPc-Fe**, where the FeOcPc-Ni CP stands out as the one with the best electrocatalytic efficiency. In contrast, the FeOcPc and FeOcPc-Fe presented the worst performance toward the OER, and the full sequence is plotted in Figure 8B. The values of the maximum turnover (TOF_{max}) and the turnover without overpotential applied are presented in both Figure 8B and Table 6.

Finally, it is important to note that Tafel slope values do not necessarily correspond to the best TOF value, although the literature commonly relates the lowest Tafel slope values with the best electrocatalyst. The TOF is a frequency value that directly corresponds to the number of turnovers the catalyst performs per second, while the Tafel values correspond to the efficiency of conversion of the electric energy provided into work. Despite the proximity of those concepts, they are not equivalent, as can be observed in Table 6, where different sequences of performance were observed for the CP materials. In fact, half of them were evaluated differently by TOF and Tafel slope, which will be used in the following section to compare the $M_aOcPc\text{-}M_b$ CPs with some commercial OER electrocatalysts.

Table 6. Values of the Maximum Turnover (TOF_{max}) and the Turnover without an Overpotential Applied (TOF_0) of each $M_aOcPc\text{-}M_b$ Material

Catalyst	Log TOF_0	Log TOF_{max}	Tafel slope (mV dec^{-1})	Efficacy order TOF/Tafel slope
CoOcPc	−5.45	7.85	74.1	6th/6th
CoOcPc-Co	−3.87	8.64	59.8	4th/4th
CoOcPc-Fe	−4.96	8.10	59.6	5th/3rd
CoOcPc-Ni	−2.78	9.20	86.4	3rd/7th
FeOcPc	−7.17	6.99	101.3	7th/8th
FeOcPc-Co	−0.58	10.27	48.2	2nd/2nd
FeOcPc-Fe	−7.16	6.99	71.1	7th/5th
FeOcPc-Ni	1.27	11.20	46.6	1st/1st

Comparison with Commercial OER Catalysts, TOF vs Tafel Slope Evaluation, and Robustness of the Material. The performance results were compared using the traditional Tafel slopes (mV dec^{-1}) and η_{10} (mV) to evaluate the viability of the $M_aOcPc\text{-}M_b$ compared to potential commercial OER electrocatalysts found in the literature (Ni, 78 Permalloy, 45 Permalloy, Kovar, 42 Invar, and Super Invar). The conditions in which the OER was performed and the results are presented in Table 7, clearly evidencing the superior efficiency of the $M_aOcPc\text{-}M_b$ materials, especially considering the lower concentration of alkali in our OER performance test (1.0 M KOH vs 0.85 M KOH). Despite the fact that CP materials present a higher η_{10}, excluding the FeOcPcNi, the Tafel slope values were superior in general, thus suggesting a more efficient conversion of energy into work. Finally, an interesting

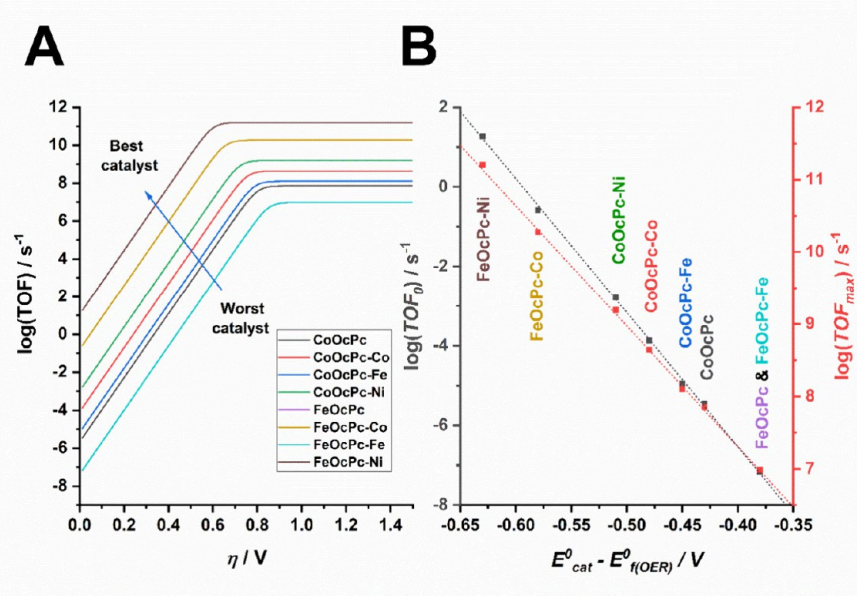

Figure 8. (A) Catalytic Tafel plots (logarithm of the TOF as a function of the overpotential). (B) Logarithm of the TOF_0 and logarithm of the TOF_{max} as a function of the difference of the formal potential in the presence of the catalyst and the thermodynamic formal potential of the OER ($E^0_{cat} - E^0_{f(OER)}$).

https://doi.org/10.1021/acsaem.4c02297
ACS Appl. Energy Mater. XXXX, XXX, XXX−XXX

Table 7. Comparison of Some Commercial OER Catalysts from Literature and the $M_aOcPc\text{-}M_b$ Materials

Catalyst	Medium	η_{10} (mV)	Tafel slope (mV dec^{-1})	β	Ref
CoOcPc	KOH 0.85 M	463	74.1	0.78	This work
CoOcPc-Co	KOH 0.85 M	388	59.8	0.96	This work
CoOcPc-Fe	KOH 0.85 M	457	59.6	0.96	This work
CoOcPc-Ni	KOH 0.85 M	370	86.4	0.67	This work
FeOcPc	KOH 0.85 M	516	101.3	0.57	This work
FeOcPc-Co	KOH 0.85 M	352	48.2	1.19	This work
FeOcPc-Fe	KOH 0.85 M	504	71.1	0.81	This work
FeOcPc-Ni	KOH 0.85 M	299	46.6	1.24	This work
Ni	KOH 1.0 M	364	71	0.81	63
78 Permalloy	KOH 1.0 M	332	54	1.07	63
45 Permalloy	KOH 1.0 M	341	61	0.94	63
Kovar	KOH 1.0 M	324	51	1.13	63
42 Invar	KOH 1.0 M	344	63	0.91	63
Super Invar	KOH 1.0 M	343	65	0.89	63

perspective would be to test the TOF of the commercial materials performing OER also, to allow a more realistic comparison in terms of efficacy.

Since the $M_aOcPc\text{-}M_b$ compounds show potential as commercial catalysts, their robustness was evaluated considering the FeOcPc-Ni material which presented the best TOF_{max}. The material was shown to be stable after up to 15 h performing the OER continuously, according to the analyses by chronopotentiometry, linear sweep voltammetry, and UV–vis spectra. The initial material and that after 15 h presented only slight changes, thus demonstrating great robustness and durability, as presented in Figures S6–S8.

CONCLUSIONS

Cobalt and iron octacarboxyphthalocyanines-based $M_aOcPc\text{-}M_b$-type coordination polymers (where $M_a = Fe^{2+}$ or Co^{2+} and $M_b = Fe^{2+}$, Co^{2+} or Ni^{2+}) were prepared and characterized and their OER electrocatalytic properties evaluated using an experimental/theoretical approach. The eight evaluated materials exhibited electrocatalytic activity, but FeOcPc-Ni stands out as the best one considering both performance and durability, with η_{10} = 299 mV at ν = 0.020 V s^{-1} and Tafel slope = 46.4 mV dec^{-1}. A more detailed analysis of their voltammetric profiles as well as Tafel, foot of the wave, turnover frequency, and impedance spectroscopy analyses indicated that the mechanism involves the formation of a peroxide intermediate where the rate-determining step can be either (a) the adsorption of the substrate (hydroxide ion or water) or (b) the regeneration of the catalyst at the end of the OER process in a competitive fashion, thus obeying the Sabatier principle as a function of the potential scan rate. Moreover, in high enough alkali concentration media, the OER mechanism is "locked" and the rate-limiting step is the irreversible proton transfer coupled to the substrate oxidation. In short, the coordination of transition metal ions generating coordination polymers can induce synergic effects, boosting the electrocatalytic properties. It was also shown that the TOF analysis combined with the FOWA can be a powerful tool, especially when associated with the analyses of the voltammetric and electrochemical impedance spectroscopy profiles, to evaluate the performance and mechanism of electrocatalytic materials.

ASSOCIATED CONTENT

Supporting Information

The Supporting Information is available free of charge at https://pubs.acs.org/doi/10.1021/acsaem.4c02297.

Additional information regarding the equivalent circuits fitting the EIS data of the MaOcPc-Mb materials at the OER potential; LSV used to determine the traditional Tafel slopes; FOWA providing the $k_{cat(app)}$ of each MaOcPc-Mb material; catalyst robustness characterization by chronopotentiometry; and voltammetric and UV–vis evaluation after 15 h of continuous OER performance (PDF)

AUTHOR INFORMATION

Corresponding Authors

Raphael P. Bacil – *Instituto de Química, Universidade de São Paulo, São Paulo, SP 05508-900, Brazil;* orcid.org/0000-0001-8742-2158; Email: bacil@iq.usp.br

Koiti Araki – *Instituto de Química, Universidade de São Paulo, São Paulo, SP 05508-900, Brazil;* orcid.org/0000-0003-3485-4592; Email: koiaraki@iq.usp.br

Authors

Ítalo R. Machado – *Instituto de Química, Universidade de São Paulo, São Paulo, SP 05508-900, Brazil*

Victor Vendruscolo – *Instituto de Química, Universidade de São Paulo, São Paulo, SP 05508-900, Brazil; The School of Chemistry, Trinity College Dublin, The University of Dublin, College Green, Dublin 2, Ireland*

Rafael M. Buoro – *Instituto de Química de São Carlos, Universidade de São Paulo, São Carlos, SP 13566-590, Brazil;* orcid.org/0000-0002-7458-3611

Helton P. Nogueira – *Instituto de Química, Universidade de São Paulo, São Paulo, SP 05508-900, Brazil*

Robson R. Guimarães – *Instituto de Química, Universidade de São Paulo, São Paulo, SP 05508-900, Brazil*

Sergio H. Toma – *Instituto de Química, Universidade de São Paulo, São Paulo, SP 05508-900, Brazil*

Márcia C. A. Fantini – *Instituto de Física, Universidade de São Paulo, São Paulo, SP 05508-090, Brazil*

Josué M. Gonçalves – *Mackenzie Instituto de Pesquisa em Grafeno e Nanotecnologias (MackGraphe), Universidade Mackenzie Presbiteriana, São Paulo, SP 01302-907, Brazil*

Complete contact information is available at: https://pubs.acs.org/10.1021/acsaem.4c02297

Funding

The Article Processing Charge for the publication of this research was funded by the Coordination for the Improvement of Higher Education Personnel - CAPES (ROR identifier: 00x0ma614).

Notes

The authors declare no competing financial interest.

■ ACKNOWLEDGMENTS

The authors would like to acknowledge the Fundação de Amparo à Pesquisa do Estado de São Paulo (FAPESP) for project no. 18/21489-1, the Conselho Nacional de Desenvolvimento Científico e Tecnológico (CNPq) for project no. 304651/2021-4, Financiadora de Estudos e Projetos (FINEP) for project no. 01.23.0237.00, and scholarship with Fundação de Apoio à Universidade de São Paulo (FUSP) grant no. 4052.

■ REFERENCES

(1) Quadrelli, R.; Peterson, S. The Energy-Climate Challenge: Recent Trends in CO2 Emissions from Fuel Combustion. *Energy Policy* **2007**, *35* (11), 5938−5952.
(2) Barbir, F.; Veziroğlu, T. N.; Plass, H. J. Environmental Damage Due to Fossil Fuels Use. *Int. J. Hydrogen Energy* **1990**, *15* (10), 739−749.
(3) Nicoletti, G.; Arcuri, N.; Nicoletti, G.; Bruno, R. A Technical and Environmental Comparison between Hydrogen and Some Fossil Fuels. *Energy Convers Manag* **2015**, *89*, 205−213.
(4) Conte, M.; Di Mario, F.; Iacobazzi, A.; Mattucci, A.; Moreno, A.; Ronchetti, M. Hydrogen as Future Energy Carrier: The ENEA Point of View on Technology and Application Prospects. *Energies (Basel)* **2009**, *2* (1), 150−179.
(5) Esmaeilion, F.; Ahmadi, A.; Hoseinzadeh, S.; Aliehyaei, M.; Makkeh, S. A.; Astiaso Garcia, D. Renewable Energy Desalination; a Sustainable Approach for Water Scarcity in arid Lands. *International Journal of Sustainable Engineering* **2021**, *14*, 1916−1942.
(6) Farhana, K.; Shadate Faisal Mahamude, A.; Kadirgama, K. Comparing Hydrogen Fuel Cost of Production from Various Sources - a Competitive Analysis. *Energy Convers Manag* **2024**, *302*, 118088.
(7) Safari, F.; Dincer, I. A Review and Comparative Evaluation of Thermochemical Water Splitting Cycles for Hydrogen Production. *Energy Convers Manag* **2020**, *205*, 112182.
(8) Sahin, N. E.; Pech-Rodríguez, W. J.; Meléndez-González, P. C.; Lopez Hernández, J.; Rocha-Rangel, E. Water Splitting as an Alternative for Electrochemical Hydrogen and Oxygen Generation: Current Status, Trends, and Challenges. *Energies (Basel)* **2023**, *16* (13), 5078.
(9) Qian, Q.; Zhu, Y.; Ahmad, N.; Feng, Y.; Zhang, H.; Cheng, M.; Liu, H.; Xiao, C.; Zhang, G.; Xie, Y. Recent Advancements in Electrochemical Hydrogen Production via Hybrid Water Splitting. *Adv. Mater.* **2024**, DOI: 10.1002/adma.202306108.
(10) Sajid, M.; Qayyum, W.; Farhan, A.; Qamar, M. A.; Nawaz, H. Progress in the Development of Copper Oxide-Based Materials for Electrochemical Water Splitting. *Int. J. Hydrogen Energy* **2024**, *62*, 209−227.
(11) Miao, L.; Jia, W.; Cao, X.; Jiao, L. Computational Chemistry for Water-Splitting Electrocatalysis. *Chem. Soc. Rev.* **2024**, *53* (6), 2771−2807.
(12) Suen, N.-T.; Hung, S.-F.; Quan, Q.; Zhang, N.; Xu, Y.-J.; Chen, H. M. Electrocatalysis for the Oxygen Evolution Reaction: Recent Development and Future Perspectives. *Chem. Soc. Rev.* **2017**, *46* (2), 337−365.
(13) Pi, Y.; Zhang, N.; Guo, S.; Guo, J.; Huang, X. Ultrathin Laminar Ir Superstructure as Highly Efficient Oxygen Evolution Electrocatalyst in Broad PH Range. *Nano Lett.* **2016**, *16* (7), 4424−4430.
(14) Reier, T.; Oezaslan, M.; Strasser, P. Electrocatalytic Oxygen Evolution Reaction (OER) on Ru, Ir, and Pt Catalysts: A Comparative Study of Nanoparticles and Bulk Materials. *ACS Catal.* **2012**, *2* (8), 1765−1772.
(15) Cherevko, S.; Geiger, S.; Kasian, O.; Kulyk, N.; Grote, J.-P.; Savan, A.; Shrestha, B. R.; Merzlikin, S.; Breitbach, B.; Ludwig, A.; Mayrhofer, K. J. J. Oxygen and Hydrogen Evolution Reactions on Ru, RuO 2, Ir, and IrO 2 Thin Film Electrodes in Acidic and Alkaline Electrolytes: A Comparative Study on Activity and Stability. *Catal. Today* **2016**, *262*, 170−180.
(16) Lyons, M. E. G.; Brandon, M. P. A Comparative Study of the Oxygen Evolution Reaction on Oxidised Nickel, Cobalt and Iron Electrodes in Base. *J. Electroanal. Chem.* **2010**, *641* (1−2), 119−130.
(17) Kötz, R.; Lewerenz, H. J.; Stucki, S. XPS Studies of Oxygen Evolution on Ru and RuO2 Anodes. *J. Electrochem. Soc.* **1983**, *130* (4), 825−829.
(18) Kötz, R.; Neff, H.; Stucki, S. Anodic Iridium Oxide Films: XPS-Studies of Oxidation State Changes And. *J. Electrochem. Soc.* **1984**, *131* (1), 72−77.
(19) Risch, M.; Ringleb, F.; Kohlhoff, M.; Bogdanoff, P.; Chernev, P.; Zaharieva, I.; Dau, H. Water Oxidation by Amorphous Cobalt-Based Oxides: In Situ Tracking of Redox Transitions and Mode of Catalysis. *Energy Environ. Sci.* **2015**, *8* (2), 661−674.
(20) Wang, Y.; Zhou, T.; Jiang, K.; Da, P.; Peng, Z.; Tang, J.; Kong, B.; Cai, W.-B.; Yang, Z.; Zheng, G. Reduced Mesoporous Co $_3$ O $_4$ Nanowires as Efficient Water Oxidation Electrocatalysts and Supercapacitor Electrodes. *Adv. Energy Mater.* **2014**, *4* (16), 1400696.
(21) Zhou, D.; Li, P.; Lin, X.; McKinley, A.; Kuang, Y.; Liu, W.; Lin, W.-F.; Sun, X.; Duan, X. Layered Double Hydroxide-Based Electrocatalysts for the Oxygen Evolution Reaction: Identification and Tailoring of Active Sites, and Superaerophobic Nanoarray Electrode Assembly. *Chem. Soc. Rev.* **2021**, *50* (15), 8790−8817.
(22) Mattos-Costa, F. I.; de Lima-Neto, P.; Machado, S. A. S.; Avaca, L. A. Characterisation of Surfaces Modified by Sol-Gel Derived RuxIr1-xO2 Coatings for Oxygen Evolution in Acid Medium. *Electrochim. Acta* **1998**, *44* (8−9), 1515−1523.
(23) Smith, R. D. L.; Prévot, M. S.; Fagan, R. D.; Zhang, Z.; Sedach, P. A.; Siu, M. K. J.; Trudel, S.; Berlinguette, C. P. Photochemical Route for Accessing Amorphous Metal Oxide Materials for Water Oxidation Catalysis. *Science (1979)* **2013**, *340* (6128), 60−63.
(24) Anantharaj, S.; Kundu, S.; Noda, S. The Fe Effect": A Review Unveiling the Critical Roles of Fe in Enhancing OER Activity of Ni and Co Based Catalysts. *Nano Energy* **2021**, *80*, 105514.
(25) Gong, M.; Dai, H. A Mini Review of NiFe-Based Materials as Highly Active Oxygen Evolution Reaction Electrocatalysts. *Nano Res.* **2015**, *8* (1), 23−39.
(26) da Silva, M. I.; Machado, Í. R.; Toma, H. E.; Araki, K.; Agnes, L.; Gonçalves, J. M. Recent Progress in Water-Splitting and Supercapacitor Electrode Materials Based on MOF-Derived Sulfides. *J. Mater. Chem. A Mater.* **2022**, *10* (2), 430−474.
(27) Yu, L.; Zhu, Q.; Song, S.; McElhenny, B.; Wang, D.; Wu, C.; Qin, Z.; Bao, J.; Yu, Y.; Chen, S.; Ren, Z. Non-Noble Metal-Nitride Based Electrocatalysts for High-Performance Alkaline Seawater Electrolysis. *Nat. Commun.* **2019**, *10* (1), 5106.
(28) Tareen, A. K.; Priyanga, G. S.; Khan, K.; Pervaiz, E.; Thomas, T.; Yang, M. Nickel-Based Transition Metal Nitride Electrocatalysts for the Oxygen Evolution Reaction. *ChemSusChem* **2019**, *12* (17), 3941−3954.
(29) Biradha, K.; Goswami, A.; Moi, R. Coordination Polymers as Heterogeneous Catalysts in Hydrogen Evolution and Oxygen Evolution Reactions. *Chem. Commun.* **2020**, *56* (74), 10824−10842.
(30) Batten, S. R.; Champness, N. R.; Chen, X.-M.; Garcia-Martinez, J.; Kitagawa, S.; Öhrström, L.; O'Keeffe, M.; Paik Suh, M.; Reedijk, J. Terminology of Metal-Organic Frameworks and Coordination Polymers (IUPAC Recommendations 2013). *Pure Appl. Chem.* **2013**, *85* (8), 1715−1724.
(31) Öhrström, L. Let's Talk about MOFs—Topology and Terminology of Metal-Organic Frameworks and Why We Need Them. *Crystals (Basel)* **2015**, *5* (1), 154−162.
(32) Bennett, T. D.; Horike, S. Liquid, Glass and Amorphous Solid States of Coordination Polymers and Metal-Organic Frameworks. *Nat. Rev. Mater.* **2018**, *3* (11), 431−440.
(33) Zhang, X.; Zhao, K.; Lin, S.; Xu, Z.; Li, L. Ambient Synthesis of Iron-Nickel Amorphous Coordination Polymer Nanosheet Arrays for Highly Efficient Oxygen Evolution Electrocatalysis. *J. Alloys Compd.* **2021**, *868*, 159218.
(34) de la Torre, G.; Claessens, C. G.; Torres, T. Phthalocyanines: Old Dyes, New Materials. Putting Color in Nanotechnology. *Chem. Commun.* **2007**, No. 20, 2000−2015.

https://doi.org/10.1021/acsaem.4c02297
ACS Appl. Energy Mater. XXXX, XXX, XXX−XXX

(35) Liao, M.-S.; Scheiner, S. Comparative Study of Metal-Porphyrins, -Porphyrazines, and -Phthalocyanines. *J. Comput. Chem.* **2002**, *23* (15), 1391−1403.
(36) Sorokin, A. B. Phthalocyanine Metal Complexes in Catalysis. *Chem. Rev.* **2013**, *113* (10), 8152−8191.
(37) Ogunsipe, A. Metallophthalocyanines: Synthesis, Properties and Applications−A Review. *Trends Food Sci. Technol.* **2018**, *3*, 669−681.
(38) Gao, W.-Y.; Chrzanowski, M.; Ma, S. Metal-Metalloporphyrin Frameworks: A Resurging Class of Functional Materials. *Chem. Soc. Rev.* **2014**, *43* (16), 5841−5866.
(39) Day, N. U.; Wamser, C. C.; Walter, M. G. Porphyrin Polymers and Organic Frameworks. *Polym. Int.* **2015**, *64* (7), 833−857.
(40) Feng, L.; Wang, K.-Y.; Joseph, E.; Zhou, H.-C. Catalytic Porphyrin Framework Compounds. *Trends Chem.* **2020**, *2* (6), 555−568.
(41) Wurster, B.; Grumelli, D.; Hötger, D.; Gutzler, R.; Kern, K. Driving the Oxygen Evolution Reaction by Nonlinear Cooperativity in Bimetallic Coordination Catalysts. *J. Am. Chem. Soc.* **2016**, *138* (11), 3623−3626.
(42) Zhong, H.; Ly, K. H.; Wang, M.; Krupskaya, Y.; Han, X.; Zhang, J.; Zhang, J.; Kataev, V.; Büchner, B.; Weidinger, I. M.; Kaskel, S.; Liu, P.; Chen, M.; Dong, R.; Feng, X. A Phthalocyanine-Based Layered Two-Dimensional Conjugated Metal-Organic Framework as a Highly Efficient Electrocatalyst for the Oxygen Reduction Reaction. *Angew. Chem., Int. Ed.* **2019**, *58* (31), 10677−10682.
(43) Jia, H.; Yao, Y.; Zhao, J.; Gao, Y.; Luo, Z.; Du, P. A Novel Two-Dimensional Nickel Phthalocyanine-Based Metal-Organic Framework for Highly Efficient Water Oxidation Catalysis. *J. Mater. Chem. A Mater.* **2018**, *6* (3), 1188−1195.
(44) Sakamoto, K.; Ohno-Okumura, E. Syntheses and Functional Properties of Phthalocyanines. *Materials* **2009**, *2* (3), 1127−1179.
(45) Costentin, C. Proton-Coupled Electron Transfer Catalyst: Heterogeneous Catalysis. Application to an Oxygen Evolution Catalyst. *ACS Catal.* **2020**, *10* (14), 7958−7967.
(46) Molina, A.; González, J.; Laborda, E. Applicability of Conventional Protocols for Benchmarking of Unidirectional and Bidirectional Multi-Electron Homogeneous Molecular Catalysts beyond the Pure Kinetic Regime. *Electrochim. Acta* **2022**, *428*, 140934.
(47) Savéant, J.-M.; Costentin, C. *Elements of Molecular and Biomolecular Electrochemistry: An Electrochemical Approach to Electron Transfer Chemistry*, 2nd ed.; Wiley, 2019.
(48) Batchelor-McAuley, C. Defining the Onset Potential. *Curr. Opin Electrochem* **2023**, *37*, 101176.
(49) Hammond, G. S. A Correlation of Reaction Rates. *J. Am. Chem. Soc.* **1955**, *77* (2), 334−338.
(50) Banks, C. E.; Compton, R. G. *Understanding Voltammetry*, 3rd ed.; World Scientific Press Company, 2018.
(51) Bacil, R. P.; Garcia, P. H. M.; Serrano, S. H. P. New Insights on the Electrochemical Mechanism of Epinephrine on Glassy Carbon Electrode. *J. Electroanal. Chem.* **2022**, *908*, 116111.
(52) Li, D.; Lin, C.; Batchelor-McAuley, C.; Chen, L.; Compton, R. G. Tafel Analysis in Practice. *J. Electroanal. Chem.* **2018**, *826*, 117−124.
(53) Bacil, R. P.; de O. Marcondes Filho, E. A.; de A. Dias, K.; Portes, M. C.; de Araujo, W. R.; Oliveira-Silva, D.; dos Santos, A. A.; Serrano, S. H. P. The Chemical Interaction between the Neurotransmitter Dopamine and the Antipsychotic Drugs Olanzapine and Quetiapine. *J. Electroanal. Chem.* **2021**, *881*, 114946.
(54) Bacil, R. P.; Garcia, P. H. M.; de Araujo, W. R.; Serrano, S. H. P. Mechanism and Kinetics of Olanzapine and Quetiapine Oxidations at Glassy Carbon Electrode. *Electrochim. Acta* **2021**, *368*, 137683.
(55) Sabatier, P. La Catalyse En Chimie Organique, Librairie Polytechnique. Ch. Béranger Paris et Liège, 1920, DOI: 10.14375/NP.9782369430186
(56) Costentin, C.; Savéant, J. M. Towards an Intelligent Design of Molecular Electrocatalysts. *Nat. Rev. Chem.* **2017**, *1* (11), 1−8.
(57) Wan, W.; Wei, S.; Li, J.; Triana, C. A.; Zhou, Y.; Patzke, G. R. Transition Metal Electrocatalysts Encapsulated into N-Doped Carbon Nanotubes on Reduced Graphene Oxide Nanosheets: Efficient Water Splitting through Synergistic Effects. *J. Mater. Chem. A Mater.* **2019**, *7* (25), 15145−15155.
(58) Laschuk, N. O.; Easton, E. B.; Zenkina, O. V. Reducing the Resistance for the Use of Electrochemical Impedance Spectroscopy Analysis in Materials Chemistry. *RSC Adv.* **2021**, *11* (45), 27925−27936.
(59) Ikeda, H.; Misumi, R.; Nishiki, Y.; Kuroda, Y.; Mitsushima, S. A Dual Bubble Layer Model for Reactant Transfer Resistance in Alkaline Water Electrolysis. *Electrochim. Acta* **2022**, *430*, 141053.
(60) Eikerling, M.; Kornyshev, A. A. Electrochemical Impedance of the Cathode Catalyst Layer in Polymer Electrolyte Fuel Cells. *J. Electroanal. Chem.* **1999**, *475* (2), 107−123.
(61) Costentin, C.; Drouet, S.; Robert, M.; Savéant, J.-M. Turnover Numbers, Turnover Frequencies, and Overpotential in Molecular Catalysis of Electrochemical Reactions. Cyclic Voltammetry and Preparative-Scale Electrolysis. *J. Am. Chem. Soc.* **2012**, *134* (27), 11235−11242.
(62) Costentin, C.; Savéant, J.-M. Multielectron, Multistep Molecular Catalysis of Electrochemical Reactions: Benchmarking of Homogeneous Catalysts. *ChemElectroChem.* **2014**, *1* (7), 1226−1236.
(63) Zetao, X.; Quintero, D.; Kitano, S.; Nagao, T.; Iwai, M.; Aoki, Y.; Fushimi, K.; Habazaki, H. Preparation of Highly Active and Durable Electrodes for Alkaline Water Electrolysis by Anodizing of Commercial FeNi and FeNiCo Alloys. *Electrochim. Acta* **2024**, *491*, 144352.

https://doi.org/10.1021/acsaem.4c02297
ACS Appl. Energy Mater. XXXX, XXX, XXX−XXX